Journal of Energy Storage 92 (2024) 112218

Contents lists available at ScienceDirect

Journal of Energy Storage

journal homepage: www.elsevier.com/locate/est

Research Papers

Enhancing operational stability of a reversible pump-turbine through blade lean design

Giacomo Zanetti [a,b,*], Giovanna Cavazzini [a], Alberto Santolin [b], Francesco Nascimben [a]

[a] Department of Industrial Engineering, University of Padova, Via Venezia 1, 35131 Padova, Italy
[b] 45 Engineering S.r.l. – Corte delle Filande 16, 36075 Montecchio Maggiore, Italy

ARTICLE INFO

Keywords:
Pumped-hydropower
Pump-turbine
S-shape
Blade lean
Rotating stall
Interblade vortexes

ABSTRACT

To provide the flexibility required by the evolving electrical grid, reversible pump-turbines (RPT) nowadays are required to rapidly switch operating mode and to operate at deep partial loads currently affected by strong fluid-dynamic instabilities. Despite these urgent needs, the design strategy of RPTs is still lacking of an effective way to mitigate the unstable behaviour in these zones, which are avoided for the negative influence on the machine operability and longevity.

This paper is aimed at defining design guidelines for facing this challenge and it presents an in-depth investigation of the influence of the blades lean angle on the RPT unstable behaviour. Considering performances, pressure and force pulsations, five runners with different blade leaning distribution (high negative, positive, curved negative, curved positive) were numerically analysed and compared with the original geometry (no lean) during the transition from a partial load to the zero-discharge condition. As a results, the close relation between the hydrodynamic instability and runner blades lean is demonstrate.

All configurations showed the development of a rotating stall at a certain point during the transition but highlighted different intensities of the phenomenon and different onset points. In particular, among the five geometries, the runner with the positive lean distribution proved to be particularly resilient to pressure and force perturbations associated with the full development of the rotating stall, significantly improving the machine behaviour in the unstable region of the characteristic curve.

1. Introduction

Hydropower encompasses 97 % of the current energy storage facilities in the European Union [1] and boasts an approximate worldwide installed capacity of 130 GW [2]. Pumped hydro energy storage (PHES) stands out among the available energy storage systems, thanks to its high round-trip efficiency (ranging from 75 % to 85 %) and competitive costs (approximately 600–1000 euros per kW) [3]. Beyond its core function, pumped hydro also enhances grid stability by providing ancillary services. It responds promptly to load variations in the electrical grid, ensuring both grid frequency and voltage regulation. However, single reversible pump-turbines (RPTs), the dominant configuration in PHES nowadays for to their cost-effectiveness [4], suffers from the rapidly switches between generating and pumping modes to meet grid demands and from the frequent start and stop requiring operation in deep off-design conditions for extended periods [5]. Indeed, RPTs are characterized by intrinsic instability, which can impact the turbine operation, particularly when it approaches the runaway condition. As a result, the time required for synchronization with the grid frequency during the start-up procedure may increase, leading to switching times unsuitable for fast regulation services.

As extensively discussed in the literature [6], the unstable behaviour of RPTs is closely linked to local inflections occurring in the machines characteristic curve, particularly in turbine mode near the runaway condition, known as S-shaped characteristic curve (where $dH/dQ < 0$) [7]. More specifically, the system exhibits unstable behaviour when the slope of the machines head-discharge curve is not only negative but also greater than the slope of the system head loss curve.

Within the S-shaped region of the machine characteristic curve, for a fixed rotational speed, the system can potentially operate at three different discharge values. This situation can lead to alternating switches between generating and reverse pumping modes, resulting in significant fluctuations in torque, head, and discharge. The subsequent occurrence of severe system vibrations [8] and pressure fluctuations in

* Corresponding author at: Department of Industrial Engineering, University of Padova, Via Venezia 1, 35131 Padova, Italy.
E-mail addresses: giacomo.zanetti.4@phd.unipd.it, giacomo.zanetti@45-eng.com (G. Zanetti).

https://doi.org/10.1016/j.est.2024.112218
Received 15 February 2024; Received in revised form 28 April 2024; Accepted 20 May 2024
Available online 30 May 2024

the machine components and penstocks can significantly reduce the runner lifespan and damage the entire power plant [9,10]. Furthermore, in this operating zone, the rotational speed of RPTs experiences significant oscillations and cannot be stabilized, causing the above-mentioned synchronization issues.

Many researchers agree that the changing slope of the characteristic curve is related to the development of rotating stall phenomena (RS), affecting the runner and the bladeless gap between the runner and the guide vanes with a frequency between 50 and 70 % of the runner rotational speed [11]. Over the years, the link between RS and the negative slope of the characteristic curve has been established through both experimental and numerical methods [12–18]. For a more extensive review of the RS phenomena, readers are encouraged to refer to [19].

The root causes of this unstable behaviour can be traced back to the design strategy, which prioritizes the pumping mode due to its larger sensitivity to flow detachment, forcing the machine to operate in turbine mode under off-design conditions across its entire operational range. An observation reinforcing the influence of the design strategy is that, even under identical operating conditions, Francis turbines do not exhibit comparable instability and oscillations. Nevertheless, the connection between the onset of the RS and the runner geometrical features remains unclear. Various geometrical modifications have been proposed over the years, primarily focusing on the guide vane and runner geometry. Xiao et al. [20] conducted an experimental and numerical study on the use of misaligned guide vanes (MGV) in a pump turbine during the start-up procedure in turbine mode. They found that MGVs can eliminate the S-curve characteristic, but at the same time, they significantly increase the unbalanced radial force on the runner during startup. Zhiwei et al. [21] investigated the hydrodynamics of a pump turbine in pump mode featuring guide vanes with bio-inspired leading-edge protuberances, finding positive effects on the hump characteristic.

Regarding the influence of the runner geometry, Olimstad et al. [22] investigated the influence of the blade leading edge profile on the unstable behaviour of a high-head pump-turbine finding that smaller blade angles result in a less steep characteristic in turbine mode with a more-pronounced S-shape in turbine brake- and pumping modes. Yin et al. [23] found that broadening the meridional channel can positively affect the unstable behaviour at partial loads in turbine mode.

Zhu et al. [24] investigated the fluid flow characteristic of two RPTs with large negative and positive lean angles founding that the negative blade lean could reduce the pressure fluctuations in the vaneless region between runner and guide vanes by controlling the flow separation on the runner blades high pressure side. In the same direction, Ye et al. [25] found that a large blade lean angle could alleviate the positive slope of the machine characteristic curve in the hump region in pumping mode. Ouyang et al. [26] demonstrated that the runner with a zero-blade lean was characterized by stronger pressure pulsations in the runner and guide vanes than those with positive or negative blade lean angles. So, it is evident that a suitable blade lean can reduce pressure fluctuations in the pump-turbine in both pumping and turbine modes, but its correlation with the S-Shape characteristic has still not been investigated.

Indeed, what is apparent from the literature analysis is that many authors investigated the adoption of the blade lean angle but mainly regarding the pumping mode for efficiency purpose and for reducing the pressure pulsations caused by the rotor-stator interaction disregarding the potential negative/positive effects in turbine mode. While the impact of the impeller blade lean angle on the hydrodynamics of pumps has been extensively explored in the literature, since the lean angle suppresses the onset of secondary flows during the flow deceleration in the relative reference system, its adoption in hydraulic turbines has not been considered due to the more stable flow field.

Most recently, only few authors started to analyze the influence of the lean angle on the turbine mode hydrodynamic instability. In 2018 Zhou et al. [27] numerically investigated the runaway oscillation process of two RPTs geometry, one with zero-lean configuration and the other with slight positive lean angle. The results showed that the onset of backflow vortex structures at the runner leading edge around the no-load point led to the sharp change in the energy dissipation rate then making the slope of dynamic trajectory positive and the runaway oscillation self-excited for both the geometries. Nevertheless, the runner with positive lean manifested the occurrence of the backflow vortex structures only at the midspan of the runner inlet hence sensibly improving the runaway oscillations. Nevertheless, as pointed by the authors, the root cause of its instability is still unclear.

Ma et al. [28] investigate in a coupled experimental and numerical campaign the pump-mode performances of two RPTs characterized by large negative and positive blade lean angle finding that the interaction between the vortexes generated in the inlet of the runner and the backflow from the outlet blocks the runner channel are related to the onset of the rotating stall phenomena developing in the turbine brake area in both runners. Moreover, the runner with high positive blade lean angle was characterized by reduced pressure fluctuation compared to the other geometry. In a following paper, Ma et al. [29] extend the previous analysis by including a third runner characterized a zero-lean configuration. As results, a different sensitivity to the vaneless space pressure pulsations linked to flow instabilities detected when the machines operated within the s-shape operating area was detected between the different runner geometries hence highlighting the correlation between pressure pulsations and blades lean configurations.

Despite the promising outcomes of prior research, a comprehensive characterization of the influence of this critical design parameter has yet to be proposed.

The main objective of this paper is to analyze the influence of the runner blade lean angle on the onset and development of flow unsteadiness in a reversible pump-turbine operating during the transition to the zero-discharge condition at a fixed rotational speed and guide vanes opening. Specifically, five different configurations of runner blade angles have been simulated to provide useful guidelines for the design of the next-generation pump-turbines.

The paper is organized as follows: in Section 2, the numerical model of the RPT is presented; Section 3 reports the results of the model validation by comparing the numerical with the experimental results in stable operating conditions; in Section 4 the results of the spectral and time-frequency analyses of the forces and pressure fields are presented and discussed for five different distributions of the runner blade lean angle. Finally, in Section 5, the fluid field comparative analysis between two representative runner geometries is presented.

2. Numerical model

2.1. Mesh generation

The first stage of a two-stage low-specific-speed Francis pump-turbine model test (ns = 37.6 rpm $m^{3/4}s^{-1/2}$) of the TES Hydraulic Laboratory of the University of Padova (Fig. 1), whose main information are reported in Tables 1 and 2, was investigated via unsteady incompressible turbulent flow numerical simulation of the machine fluid domain by means of the commercial software ANSYS 22.0.

In the analysed configuration the radial gap between the trailing edge of the guide vanes and the runner tip was equal to 10.5 mm, corresponding to 5.25 % of the impeller radius. The relative azimuthal position between stay and guide vanes was fixed to +8 deg. of alignment. Since the goal of this study is to evaluate the unstable behaviour in the S-Shape portion of the characteristic curve, a guide vane opening angle of 18° was chosen, as it is associated with this unstable behaviour, even in pumping mode [30].

The entire fluid passage was divided in five domains and structured meshes were adopted to discretize draft tube, impeller, guide vanes, bladed return channel and leakage system. Fig. 2 reports the meridional scheme of the model. The commercial software ICEM CFD was adopted for the discretization of the return channel, leakage system and draft

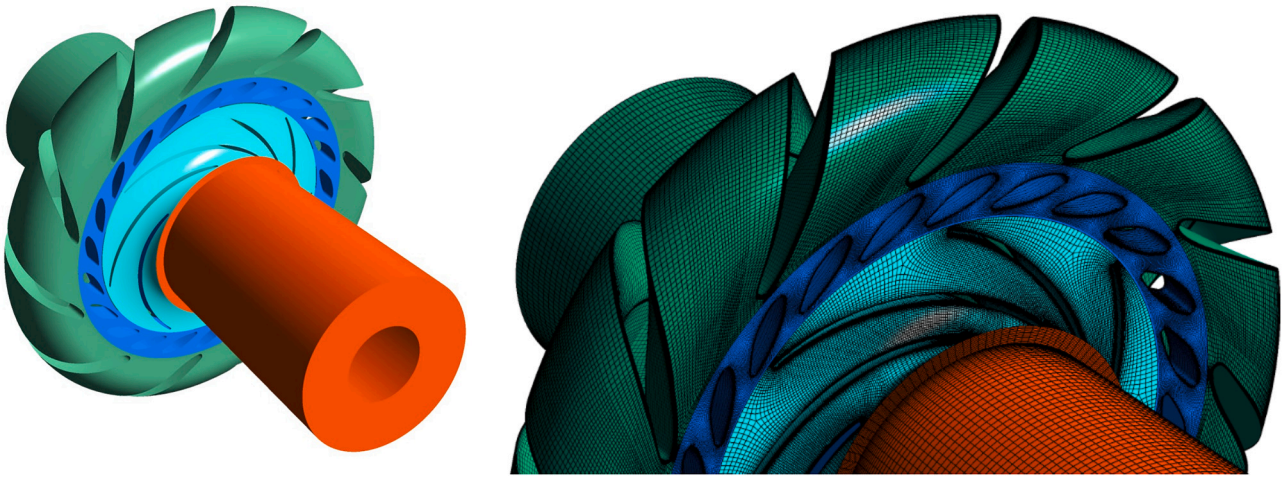

Fig. 1. Computational fluid domain and mesh.

Table 1
Geometry characteristics and performance parameters of the simulated pump-turbine.

Impeller data			
D_2 [mm]	B_2 [mm]	Z_b	β_{2b} [°]
400	40	7	26.5
Guide vanes data			
D_3 [mm]	B_3 [mm]	Z_{bGV}	α_{3b} [°]
500	40	22	10–30
Return channel data			
D_4 [mm]	B_4 [mm]	Z_{bRC}	α_{4b} [°]
516	40	11	30

Table 2
Performance parameters of the simulated pump-turbine.

Specific speed	37.6 [rpm $m^{3/4}s^{-1/2}$]
Rated speed	600 [rpm]
Best efficiency discharge	110 [kg s^{-1}]
Degree of reaction at BEP ϵ_r	0.7[−]
Nominal Guide vanes opening	22.9 [°]

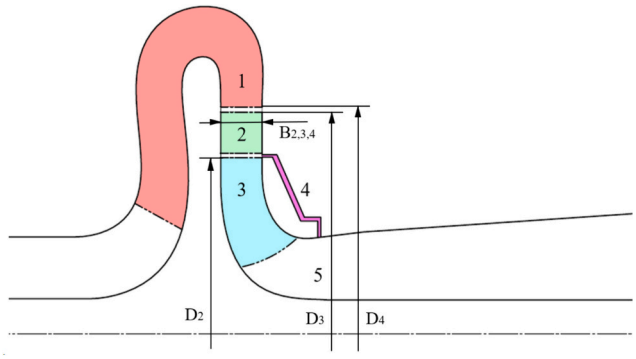

Fig. 2. Meridional view of the numerical model. Colored regions refer to the blades and leakage system: 1) return channel; 2) guide vanes; 3) runner; 4) front leakage; 5) draft tube.

tube domains while the runner and the guide vanes were discretized by adopting the ANSYS TURBOGRID software. To capture the boundary layer flow separation, special attention was paid to the boundary refinement of the return channel, guide vanes and runner meshes. An O-grid type mesh was adopted for the discretization of the return channel domain while an ATM optimized mesh was adopted for the runner and guide vanes domains.

Mesh independence was investigated in an initial sensitivity analysis, where the stage water head H (evaluated as total pressure difference between the inlet and outlet sections of the entire domain) and the runner torque were evaluated at 57 % of the nominal discharge using different mesh resolutions. This specific operating condition was selected to optimize the mesh for the initialization of the transient simulation of the machine toward the zero-discharge condition. Both water head and runner torque signals exhibited negligible differences once the computational domain reached 11 million nodes (as shown in Fig. 3).

Particular attention was reposed in the refinement of the runner and guide vanes meshes, resulting in a total number of 3.5 million nodes in each domain. The mesh statistics for each component are summarized in Table 3.

2.2. Numerical approach

In light of the significant flow separations expected in the fluid field, with several structures of different scale, the hybrid Scale Adaptive Simulation turbulent model (SAS-SST) was adopted for the simulations of the entire machine fluid domain. Representing a developed and improved URANS (Unsteady Reynold Navier Stokes) method, the SAS turbulent model employes the Large Eddy Simulation (LES) model within the unsteady flow regions and the Shear Stress Transport (SST) RANS model in the flow steady regions. Thanks to this approach, smaller turbulent structures can be generated with the turbulence cascade going down to the mesh size limit [31]. Due to its capability in the prediction of flow instability, the SAS model offers an attractive alternative to the existing hybrid RANS/LES methods [32] and has been already proved to be effective for the evaluation of the tridimensional behaviour of the fluid flow with several applications in the field of hydraulic turbines [16,17] [33–35].

All the interfaces between stator-rotor domains were standard transient sliding interfaces while walls were defined as no-slip smooth walls.

With regard to the boundary conditions, mass flow rates and static pressure values were imposed at the return channel inlet and the draft tube outlet section, respectively. For the inlet mass flow, a stochastic fluctuation of velocities with a 5 % free stream turbulent intensity was adopted. Moreover, at the draft tube outlet section, an opening condition was set in order to account for the expected high intensity flow field disturbance. A constant rotational speed, equal to the turbine mode

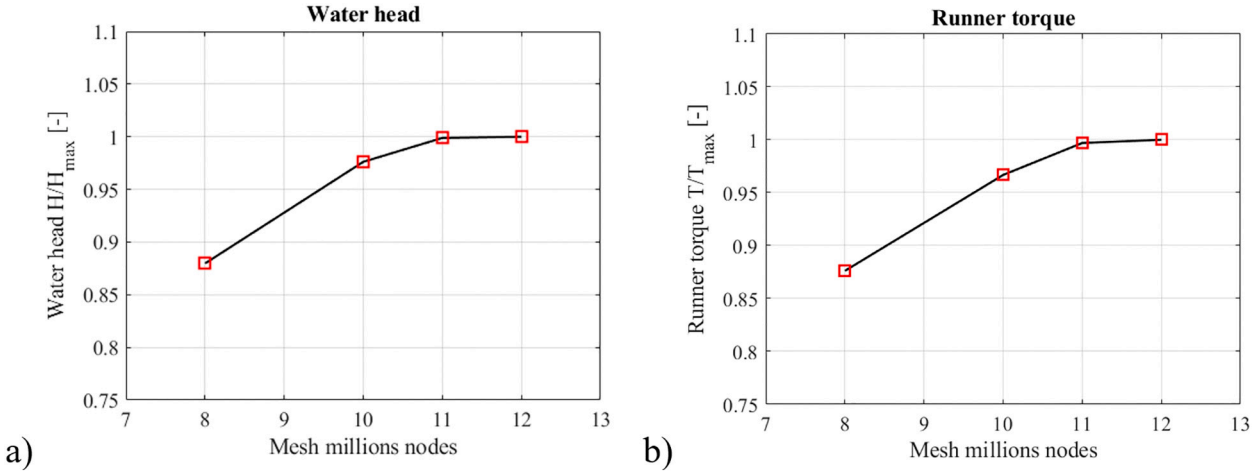

Fig. 3. Mesh convergence study: a) normalized water head; b) normalized runner torque.

Table 3
Adopted mesh statistics.

Component	Number of nodes	Ave y+	Min y+
Return Channel	3.26×10^6	20	0.08
Guide Vanes	3.45×10^6	28	0.09
Runner	3.45×10^6	30	0.035
Leakage System	4×10^5	40	0.5
Draft tube	2.42×10^5	21	0.4
Total	10.8×10^6		

nominal one, was adopted.

Regarding the timestep adoption, 1° of impeller revolution was fixed. As demonstrated by Braun [38], such approach represents a reasonable compromise between the computational effort and the solution accuracy, even in off design conditions. The root mean square Courant number was lower than 2.5 for the entire simulations, guaranteeing an accurate resolution of the transient details.

Finally, the high-resolution advection scheme of the commercial software ANSYS CFX, the second order backward Euler method for time integration was adopted. In order to maintain within acceptable limits, a maximum internal loop coefficient equal to 4 was adopted. With these simulation settings, the maximum resulting RMS values for the residuals were *u momentum* 5e-5, *v momentum* 5e-5, *w momentum* 2e-5, and *turbulence kinetic energy* 5e-5.

2.3. Validation of the numerical model

To validate the numerical approach, numerical and experimental performance curves were compared in steady conditions both in terms of water head and runner torque. The experimental data were obtained according to ISO standards from Dep. Industrial Engineering—University of Padova. The global measurements have been performed following IEC recommendations with a 0.1 % precision for head in the vicinity of the best efficiency condition. In detail the precision achieved in measuring the water head, runner torque, and speed was respectively 0.01 m, 0.2 %, and ± 0.5 rpm. Instrument calibration was conducted on-site to ensure accuracy. Reader can find more details regarding the experimental set up in [16] [36,37].

The results of this first part of the validation procedure are reported in Fig. 4 where the machine characteristic curves are reported in terms of water head and hydraulic efficiency.

Six operating points (57%Q_{bep}, 67%Q_{bep}, 76%Q_{bep}, 86%Q_{bep}, 95% Q_{bep}, 105%Q_{bep}) were investigated by performing a series of transient simulations with fixed runner speed of 600 rpm and mass flow rates. The numerical data were acquired for two impeller revolutions after >10 revolutions required to achieve a quasi-steady simulation convergence.

Numerical and experimental data were in quite good agreement in terms of water head, with a maximum error below 5 % and smaller than 3.5 % at the best efficiency discharge. Along the same lines, the hydraulic efficiency comparison showed a maximum error below 2.5 % and smaller than 2 % at the best efficiency discharge.

As reported in Fig. 4b, the head showed a tendency to smaller prediction than the experimental data above 70%Q_{bep} while an overprediction occurred at partial load. Nevertheless, the good agreement between experimental and numerical results demonstrated the capability of the numerical model to predict the performance of the pump-turbine with sufficient accuracy.

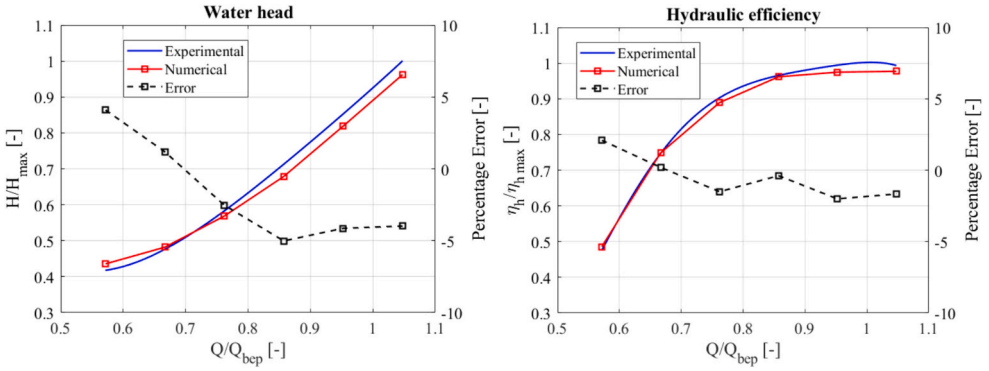

Fig. 4. Validation of the numerical model: a) water head; b) hydraulic efficiency.

2.4. Runner modification scheme

The adoption of an appropriate stacking conditions represents a typical solution for the secondary flows suppression in radial and mixed flow turbomachines. In pumps, and hence also in RPTs, linear lean of the blade trailing edge against the direction of rotation at the impeller trailing edge is usually adopted. With this approach, close to the impeller outlet section, the load decreases at the shroud and increases at the hub. Nevertheless, structural limits and manufacturing exigencies poses a limit in the lean of the blades trailing edge. Further information regarding the current techniques adopted for the secondary flows suppression can be found in [39].

In this paper, the blade lean angle θ is defined as positive when the blade profile on the runner hub rotates along the runner rotation direction, and the blade profile on the runner shroud rotates against the runner rotation direction in reference to the turbine mode rotation direction.

In the modification process of the runner blades lean angle θ, the blades profile in spanwise direction was rotated basing on the runner center. Thanks to this approach, both the blades angles in the streamwise direction, the leading edge and trailing edge curve remained unchanged. An example of the runner blades modification scheme is reported in Fig. 5. Here, the solid black line represents the original blade profile while the dashed red and blue lines represent the modified profiles at the runner hub and shroud surfaces respectively.

In this paper, in addition to the original runner, four different distributions of the lean angle in the spanwise direction have been adopted:

- Model A: negative 15° linear lean angle;
- Model B: positive 15° linear lean angle;
- Model C: negative 6° curved lean angle;
- Model D: positive 6° curved lean angle;

The modified runner geometries are reported in Fig. 6.

A value of 15° for the linear lean angle was adopted since represents a compromise between the need for increasingly high-performance turbines geometries and the manufacturing requirements. At the same time, the curved lean distribution has been designed in order to have the same lean angle slope at the runner shroud/hub as for the linear lean geometries. Thanks to this design approach, runner models A-C and B—D share the same lean slope at the shroud surface while the same lean slope occurs between runner models A-D and B—C at the hub surface.

3. Numerical analysis of the pump-turbine behaviour toward zero-discharge condition

3.1. Numerical simulations

Since this study mainly focused on the unstable behaviour associated with the machine S-shape characteristic, varying over time boundary condition was adopted in order to retrace the machine characteristic curve in the unstable region. For this purpose, the machine characteristic was retraced in a wide discharge range from 57 % of the best efficiency flow rate value (Q_{bep}) up to the zero-discharge condition.

To achieve the full development of the unsteady phenomena, which is expected to start close to the runaway condition, the simulation was performed for 60 complete runner revolutions corresponding to 6 s of simulation time. Starting in a partial load safe operating condition, the machine characteristic was retraced up to the zero-discharge condition, passing through the turbine brake area, to in-depth evaluate the onset and development of the typical fluid flow phenomena affecting the machine hydrodynamic. Therefore, a time-dependent boundary condition was set by slowly varying the mass flow rate over time at the return channel inlet section. A linear variation of the mass flow rate Q was chosen according to the following equation:

$$Q = 57\%Q_{bep} - 9.5\%Q_{bep}\, t \tag{1}$$

Guaranteeing a constant deceleration of the fluid speed at the return channel inlet section, it is possible to limit potential effects caused by the variation of the fluid inertia. Consistent with the literature on the topic, the proposed discharge variation law allows for enhancing the stability of numerical simulations [13].

3.2. Characteristic curves

To investigate the blade lean effect on the machine hydrodynamic performance in the unstable turbine mode region, the numerical characteristic in the different cases was analysed. Since the unstable behaviour is strictly related to the s-shaped trend, the local slope of the characteristic curves in the unstable branch can be adopted as representative parameter.

Fig. 7 presents the comparison between the numerical dimensionless speed–discharge characteristic curves for the different runner configurations. Speed and discharge factors are defined according to the International Electrotechnical Commission 60,193 standard as:

$$n_{ED} = \frac{nD_2}{\sqrt{gH}} \tag{2}$$

$$Q_{ED} = \frac{Q}{2D_2^2\sqrt{gH}} \tag{3}$$

where D_2 represents the impeller outlet diameter, H the water head at the machine inlet section and n the runner rotational speed.

Despite the blade lean-angle configurations clearly influence the average machine characteristic, none of the considered configurations is able to eliminate the negative-to-positive slope transition. Nevertheless, the runner model B shows an improvement in the machine unstable behaviour with a smoother and less steep characteristic compared to the original runner (with 0-lean). The model B also presents a reduction in the characteristic oscillation amplitude and this resulted to be due to the reduction of the head pulsation amplitude mainly achieved by the

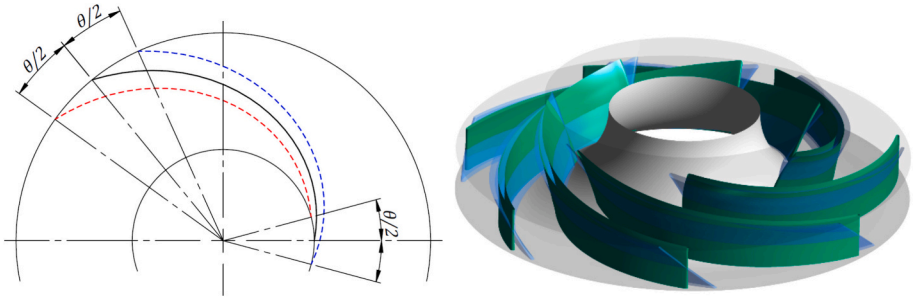

Fig. 5. Example of runner modification scheme: a) 2D prospective; b) 3D prospective and comparison with original runner. Hub: dashed red line; Shroud: dashed blue line. (For interpretation of the references to colour in this figure legend, the reader is referred to the web version of this article.)

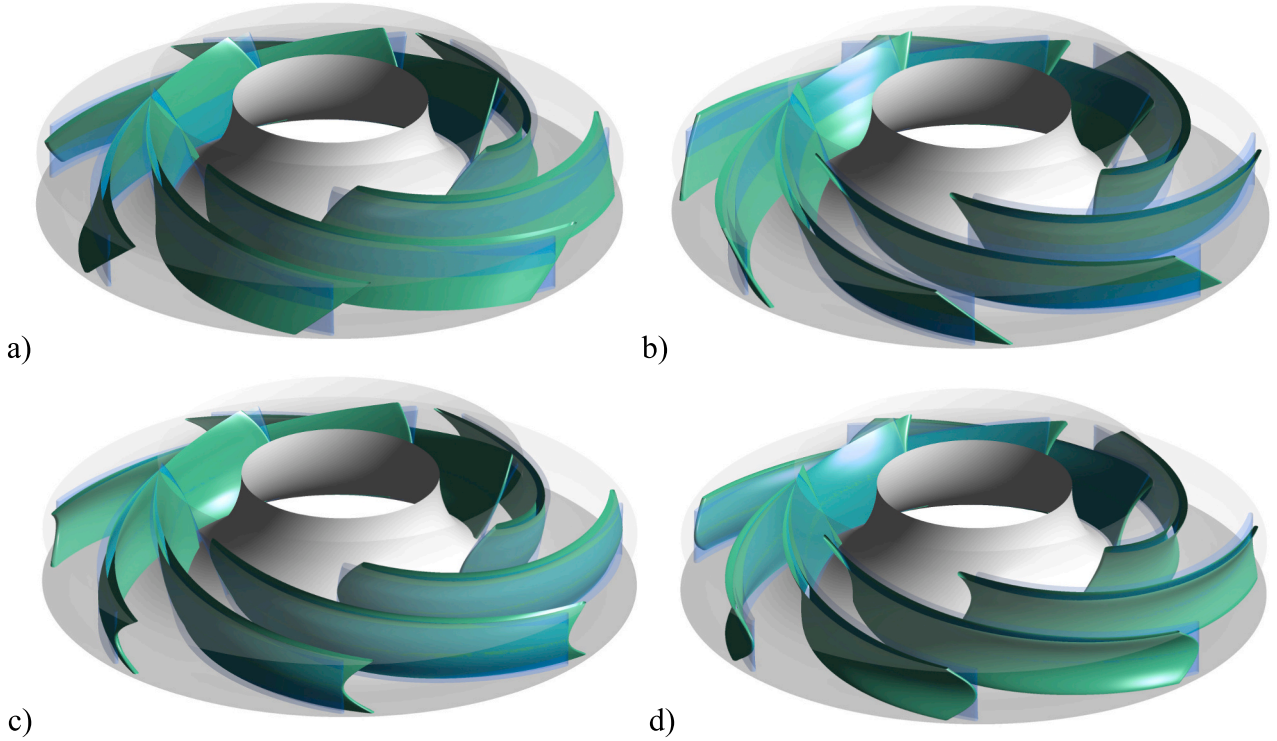

Fig. 6. Modified 3D runner geometries: a) model A: linear −15°; b) model B: linear +15°; c) model C: curved +6°; d) model D: curved −6°.

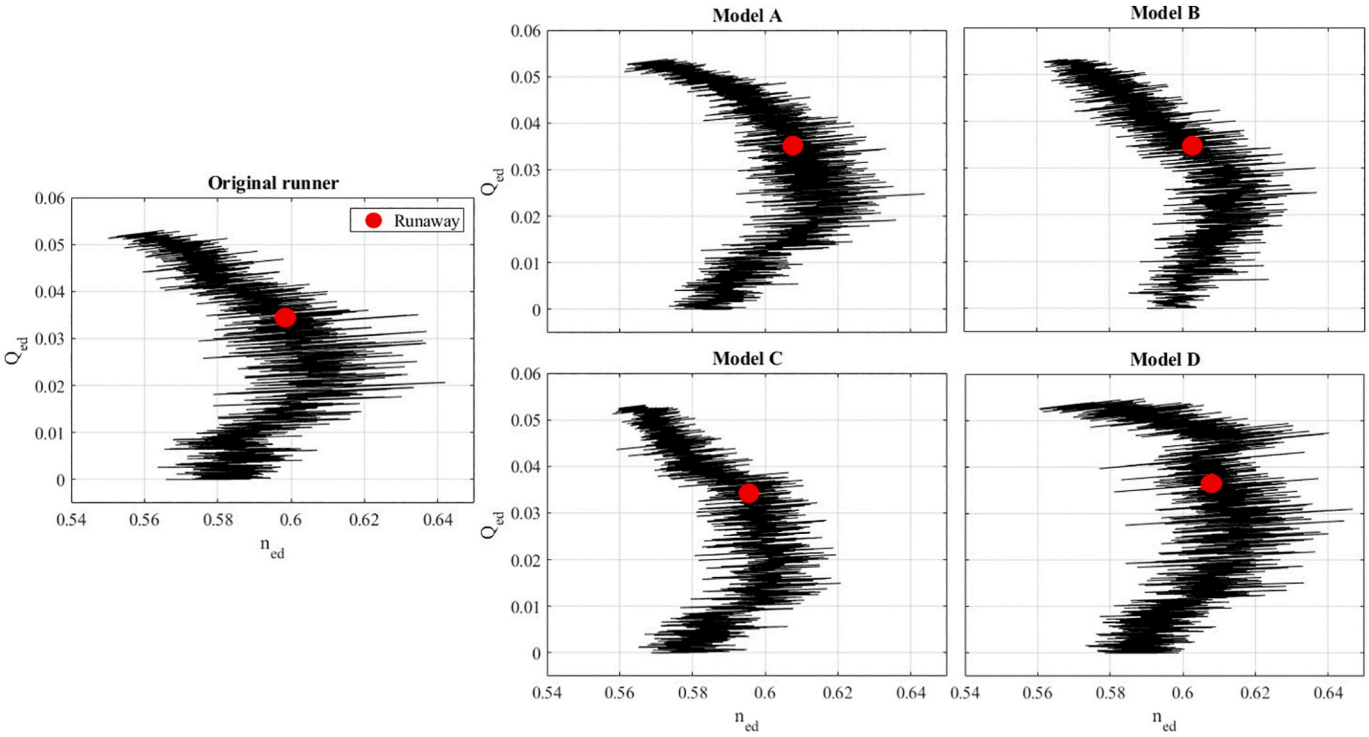

Fig. 7. Non-dimensional machine characteristic curves comparison for different runner lean-angle configurations.

improvement in the rotor-stator interaction.

A smoother slop can also be found in the runner models A and C, but with some differences. The model A presents a smaller oscillation amplitude in the negative and positive branches of the characteristic curve but greater oscillation in the negative-to-positive transition zone. In the model C, the reduction in oscillation amplitude is more generalized but the transition zone (with a zero slope) affects a wider discharge-factor range (between 0.05 and 0.1). This zone is even wider in the model D (in the range between 0.05 and 0.15 of the discharge factor), presenting a steeper characteristic curve with wider oscillations than the original geometry.

So, the comparison highlighted that, adopting a high positive blade

lean angle (model B) can limit the positive slope in the characteristic curve, while a reduction of the head pulsations can also be achieved by adopting negative angles (models A and C).

In terms of performance, all the simulated configurations show an increase in hydraulic efficiency under partial load, accompanied by a reduction in water head measurements (Fig. 8).

To understand more in depth the influence of the lean angle on the S-Shape characteristic, it was necessary to study the fluid-dynamics inside the machine components.

4. Fluid flow characterization

4.1. Fluid-dynamic phenomena spectral characterization

Since the onset of severe pressure pulsations and vibrations is related to the negative slope of the machine characteristic curve, a spectral analysis both in the frequency and time-frequency domains was performed on the numerical signals acquired during the simulation. More details on the adopted approach can be found at Pavesi et al. [40].

Fig. 9 reports the positions of the numerical signals acquired during the transition toward the runaway condition: static pressure signals (green circles) acquired at the guide vanes passages (Pgv1- Pgv22); static pressure signals (red and blue circles) in all the runner passages at midspan (P1_CH1-P6_CH1); torques acting on all the guide vanes (Tgv1-Tgv22) and runner blades (Trb1- Trb7). The data were acquired simultaneously at a frequency of 3600 Hz (time step of 1 deg. with a runner rotation rate of 600 rpm) during the entire transient simulations.

First, a Fast Fourier Transform (FFT) analysis was carried out to assess the impact of the lean on the machine pressure field in the different configurations. Because of the adoption of time-varying boundary conditions, the signals, covering a timespan equal to 6 s, were not divided into overlapping segments therefore resulting in a frequency resolution of 0.17 Hz. As the change in slope of the characteristic curves occurs only in the last portion of the signals (about 15 %), it is important to properly select the sampling window function allowing to minimize the signal power loss of the low frequency components developing at the end of the sampling period. Consequently, in contrast to the more common Hanning window, generally adopted in similar studies, a cosine bell windowing function C_b was preferred. Depending on the cosine factor r, the cosine bell window corresponds to a rectangular window for $r = 0$, while for $r = 1$ it corresponds to a Hanning window [41]. For this study a cosine factor equal to 0.15 was adopted to avoid an excessive damping of the low-frequency components at the window boundaries.

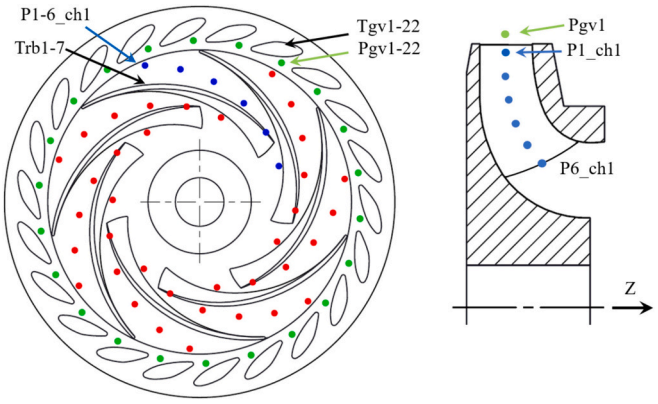

Fig. 9. Scheme of the positions of the acquired numerical signals.

Fig. 10 presents a comparative analysis of the frequency spectra of water head signals for various runner configurations. The results revealed distinctive peaks in the FFTs of the water head signals for all the simulated runners, with the exception of the runner model B. In particular, there are three distinct frequency peaks falling within the ranges of 8–18 Hz, 110–120 Hz, and 216.5–216.8 Hz, each displaying varying amplitudes dependent on the specific case. Two of the peak ranges can be attributed to the blade passage frequency (110–120 Hz) and the runner passage frequency (8–18 Hz) respectively, whereas the last perturbation (216.5–216.6 Hz) is likely due to the full development of a rotating instability affecting the machine hydrodynamic, whose presence is confirmed by the frequency spectrum of the x-direction radial forces acting on the entire runner surface (Fig. 11).

As it is clear in the figure, all the runner configurations are characterized by pronounced radial force pulsations occurring within a frequency band ranging from 3.3 to 4 Hz, which is typical of the onset and progression of the rotating instability introducing a progressive discharge unbalance [17]. It is interesting to notice that the intensity of the force pulsations (and hence of the phenomenon) varies: the models A and D exhibit behaviour closer to the original runner, with a high amplitude low-frequency signal component dominating the entire spectrum, whereas this amplitude is reduced in the model C even more in the model B.

So, as highlighted by Fig. 10, the rotating stall interacts with the guide vanes causing the pulsation in the water head frequency spectra F_{RI_H} at 216.5–216.6 Hz, resulting as a result of the difference between

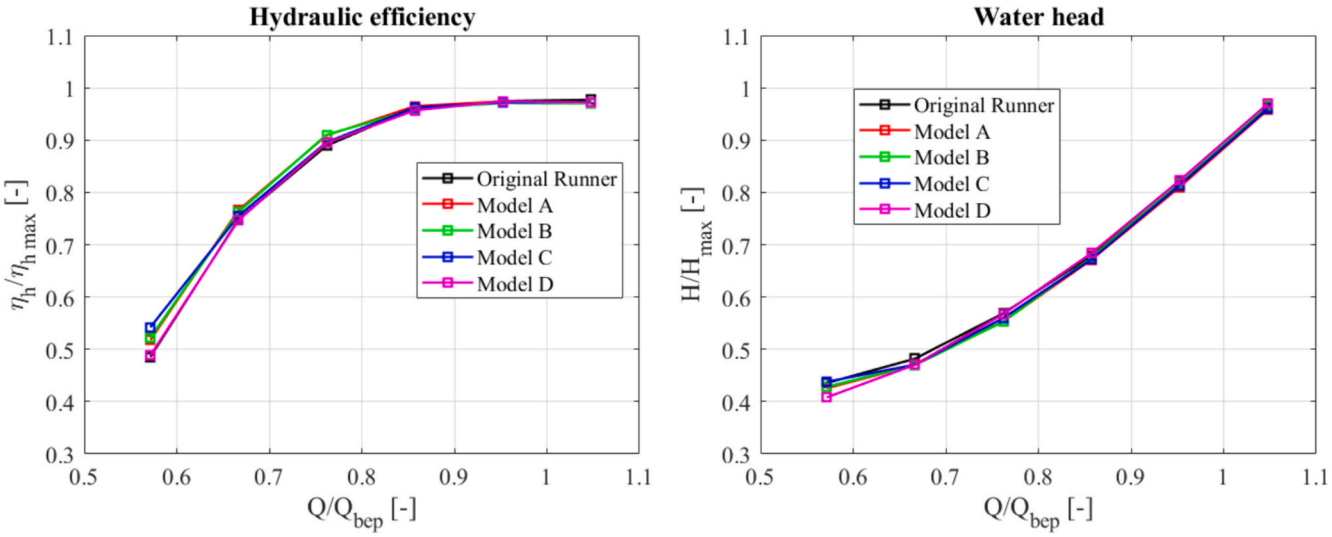

Fig. 8. Performance comparison between original and modified runners: a) water head; b) hydraulic efficiency.

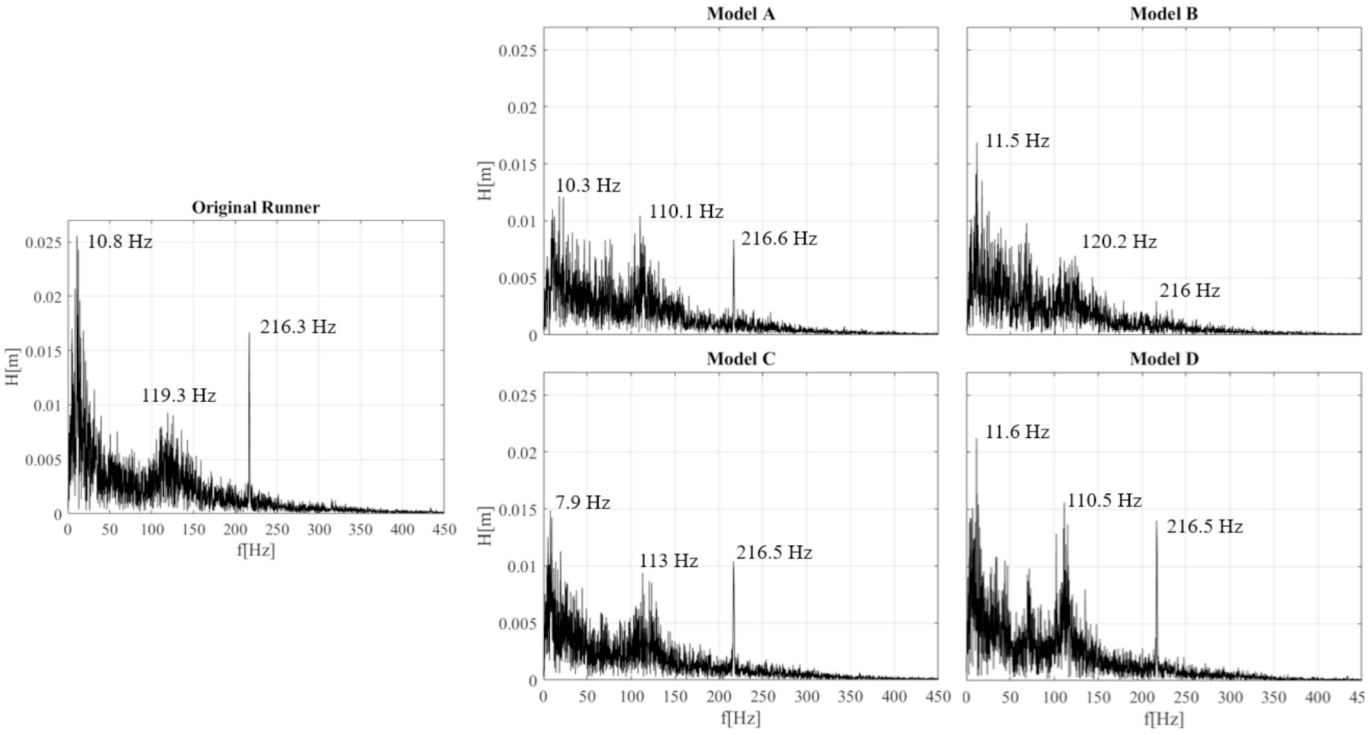

Fig. 10. FFTs of the water head signals in the different configurations.

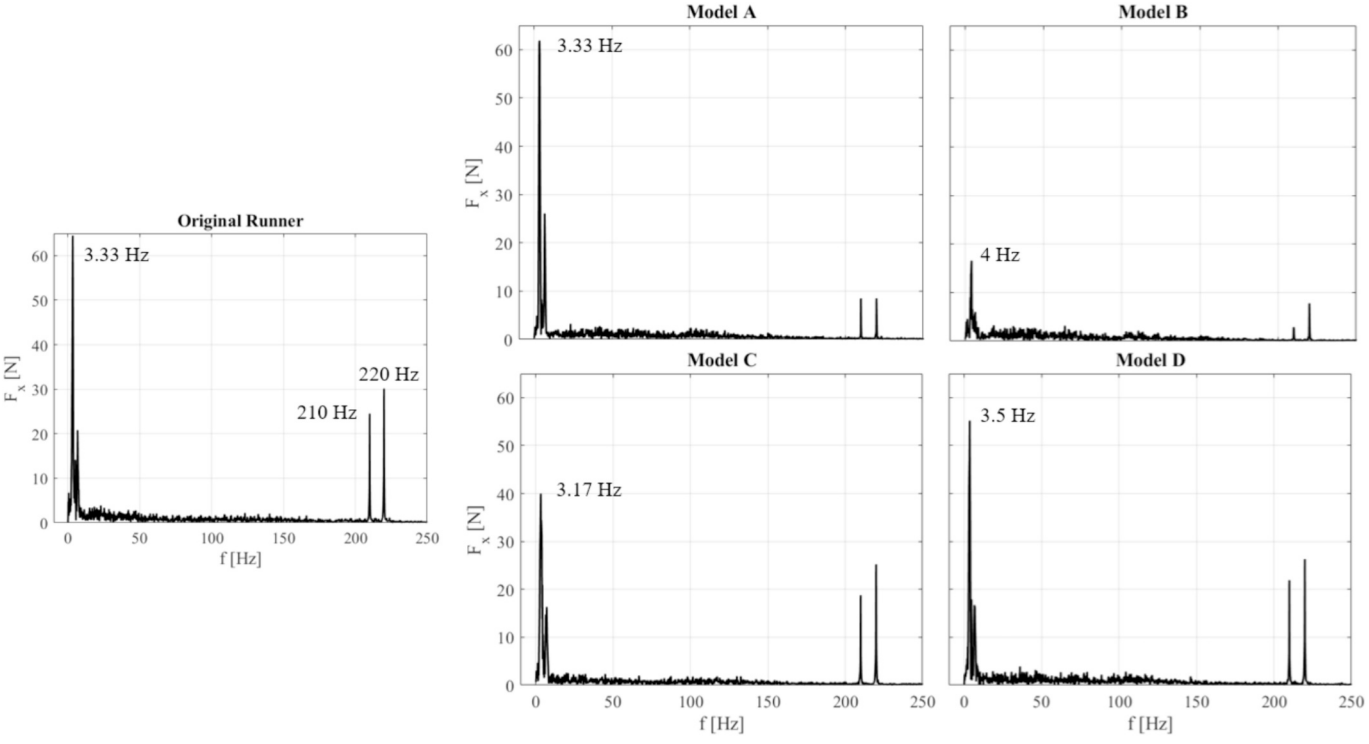

Fig. 11. Runner x-direction radial force frequency spectrum comparison.

the guide vane passage frequency BP_{GV} (220 Hz) and the rotating stall frequency F_{RI_RF} in the runner rotating frame (assuming 3.3 Hz):

$$F_{RI\_H} = BP_{GV} - F_{RI\_RF} \simeq 220\ Hz - 3.3\ Hz \simeq 216.7\ Hz \quad (5)$$

The rotating frequency of the structured instability in the stationary frame F_{RI_SF} can be evaluated by means of the runner rotation frequency F_{RR} (10 Hz) according to the following relation [42]:

$$F_{RI\_SF} = F_{RI\_RF} - F_{RR} \simeq 3.3 - 10 = -6.7\ Hz \quad (6)$$

The negative value obtained for F_{RI_SF} means that the flow disturbance moves with a sub synchronous frequency in the opposite direction of the runner rotation.

To support this hypothesis, the spectral characterization was extended to the static pressure signals acquired close to the guide vanes in a runner channel (P1_CH1). The results of such analysis are reported in Fig. 12.

All the simulated configuration, with the exception of the runner model B, are characterized by a major low frequency perturbation in a frequency band within 3.3–3.7 Hz. Simultaneously, the blade-pass frequency of the guide vanes, measuring 220 Hz, is distinctly observed in all signals. This result confirms the presence of a rotating instability affecting the runner and guide vanes hydrodynamics.

The original runner and the runner Model A appear to be more sensitive to the development of the rotating instability while Model C manifest a greater sensitivity to the stay vanes BP frequency. Conversely, the runner Model B demonstrates improved hydrodynamic behaviour, characterized by the absence of significant disturbances related to rotating instability and a lower sensitivity to interactions with the wake of the guide vanes. These findings align with the results presented in Section 3.2, where a smoother and less steep characteristic curve was associated with runner model B.

To further investigate the impact of the rotating instability on the machine hydrodynamics, a comparative analysis between the frequency spectra of the static pressure signal acquired in a runner channel (P1-6_CH1) was performed between the different runner configurations. Fig. 12 reports the comparison between the max frequency spectra amplitude of the signal frequency components in a frequency band within 3.3 Hz and 3.7 Hz.

As indicated by the water head frequency analysis, the original runner exhibits the most pronounced perturbation, with the greatest amplitude close to the leading edge, gradually decreasing along the channel. It is possible to assert that the rotating phenomena affecting the runner is characterized by a greater intensity close to the runner inlet section and hence in proximity of the guide vanes. The runner A exhibits a behaviour closer to the original model.

On the contrary, runners D and B manifested an almost constant signal amplitude in the entire channel, with smaller average amplitude in model B.

Taking into account the results reported in Figs. 11–13, it results clear how the evolution of the pressure field toward the unstable region significantly impacts the structural integrity of the runner, leading to the onset of severe torque and radial forces pulsations potentially damaging the entire machine.

Considering these outcomes, although the formation of rotating instability in the runner model B cannot be excluded, a drastic improvement in hydrodynamic behaviour associated with a significant decrease in pressure and force pulsations can be observed.

Moreover, all the configurations show other two frequency peaks respectively at 210 and 220 Hz, with close amplitudes, due to the combination of the runner rotational frequency (10 Hz) and the guide vane rotor stator interaction (220 Hz). Anyway, in accordance with existing literature, from this analysis is possible to confirm how the adoption of large blade lean angles can significantly mitigate the pulsations stemming from rotor-stator interaction effects.

4.2. Time-frequency characterization: influence of the lean

Despite the analysis in the frequency domain allows to reach a great accuracy in the identification of the relevant frequencies related to the flow unsteadiness, the disregarded time information partially biases the amplitude comparison, since the influence of the unsteady phenomena is expected to grow only in the last part of the signals. To identify the operating condition in which the frequency characterizing the rotating instability appears, a time–frequency characterization was performed via wavelet transform analysis.

The continuous wavelet transform W was computed according to the following definition:

$$W(a,b;f(t),\psi(t)) = \int_{-\infty}^{\infty} f(t)\frac{1}{a}\psi^{*}\left(\frac{t-b}{a}\right)dt \tag{6}$$

where Ψ(t)* represents the complex conjugation of the wavelet function, f(t) the signal being analysed, a and b represent respectively the wavelet scale and position parameters. In our study the complex Morlet wavelet with $2\pi f_0 = 8$ was adopted as mother wavelet [43]. Each wavelet spectrum presents the so-called “cone of influence”, delimiting with a

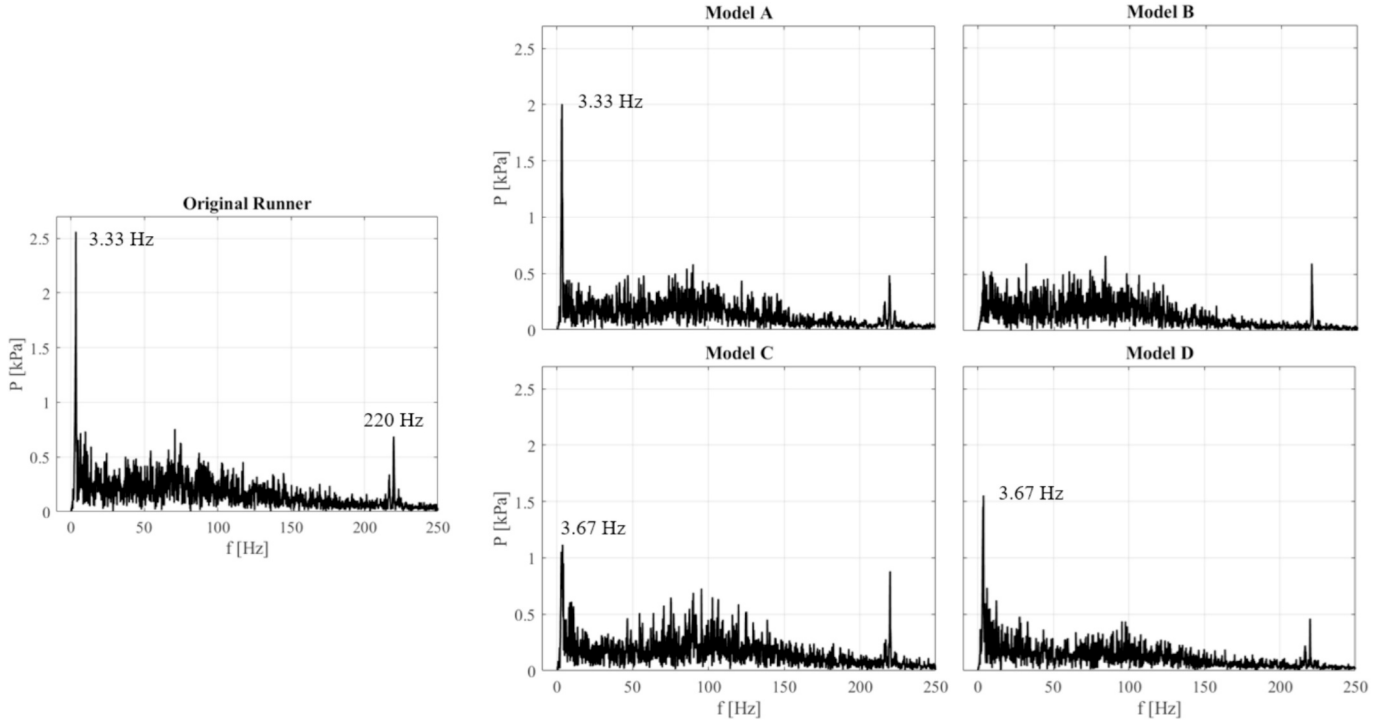

Fig. 12. Runner channel pressure signals (P1_CH1) frequency spectrum comparison.

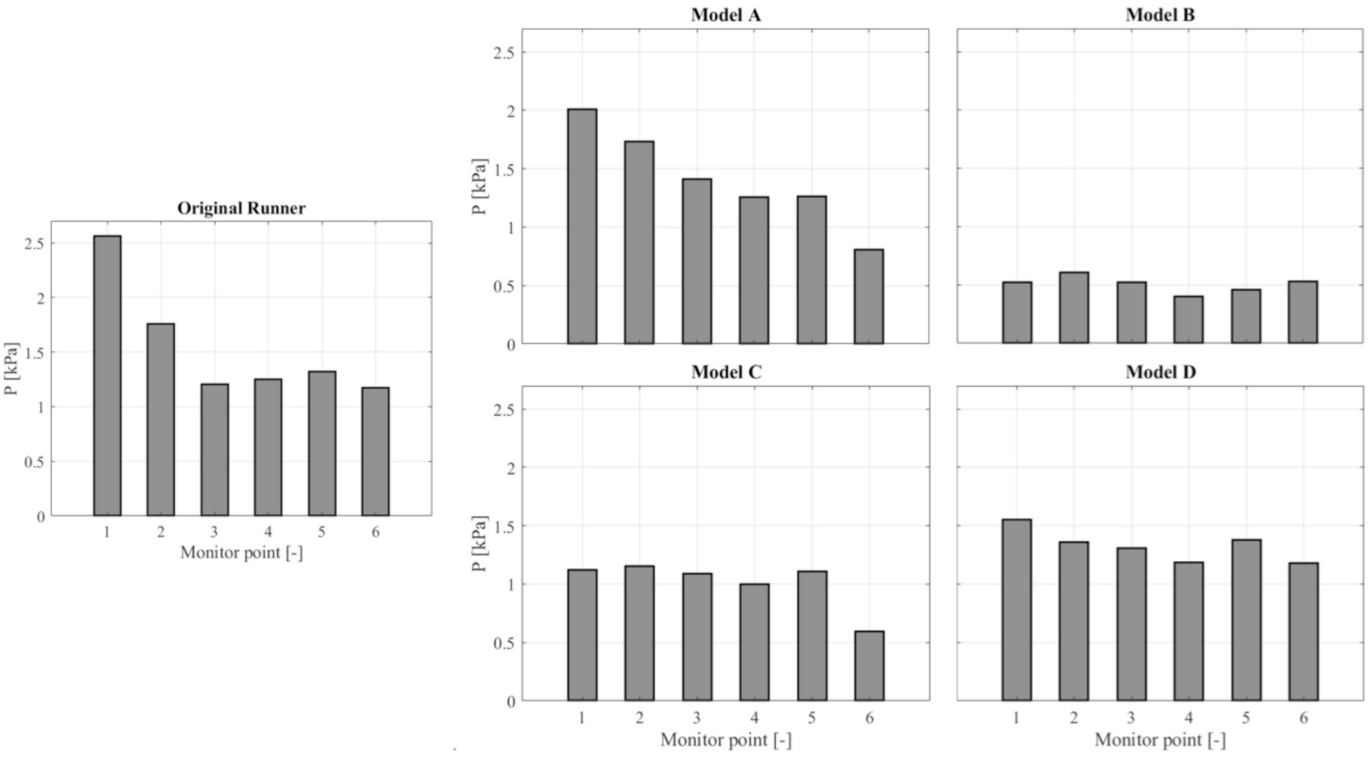

Fig. 13. Runner pressure signals (P1-6_CH1) low frequency perturbation amplitude comparison.

broken line the region of the spectrum in which errors could occur because of the finite-length time of the considered signals.

To support the analysis of the water head signal reported in Fig. 10, Fig. 14 shows the comparison between the water head signal wavelets for the different runner configurations. Regarding the original runner geometry, the time-frequency analysis clearly shows that the high frequency phenomena occurring in the water head frequency spectrum at 216.6 Hz (Fig. 10) appears approximately starting from 12%Q_{bep}. This result highlights the correlation between this peculiar pressure perturbation and the evolution of the fluid filed toward the zero-discharge condition demonstrating how the full development of the rotating stall only occurs within a specific discharge range.

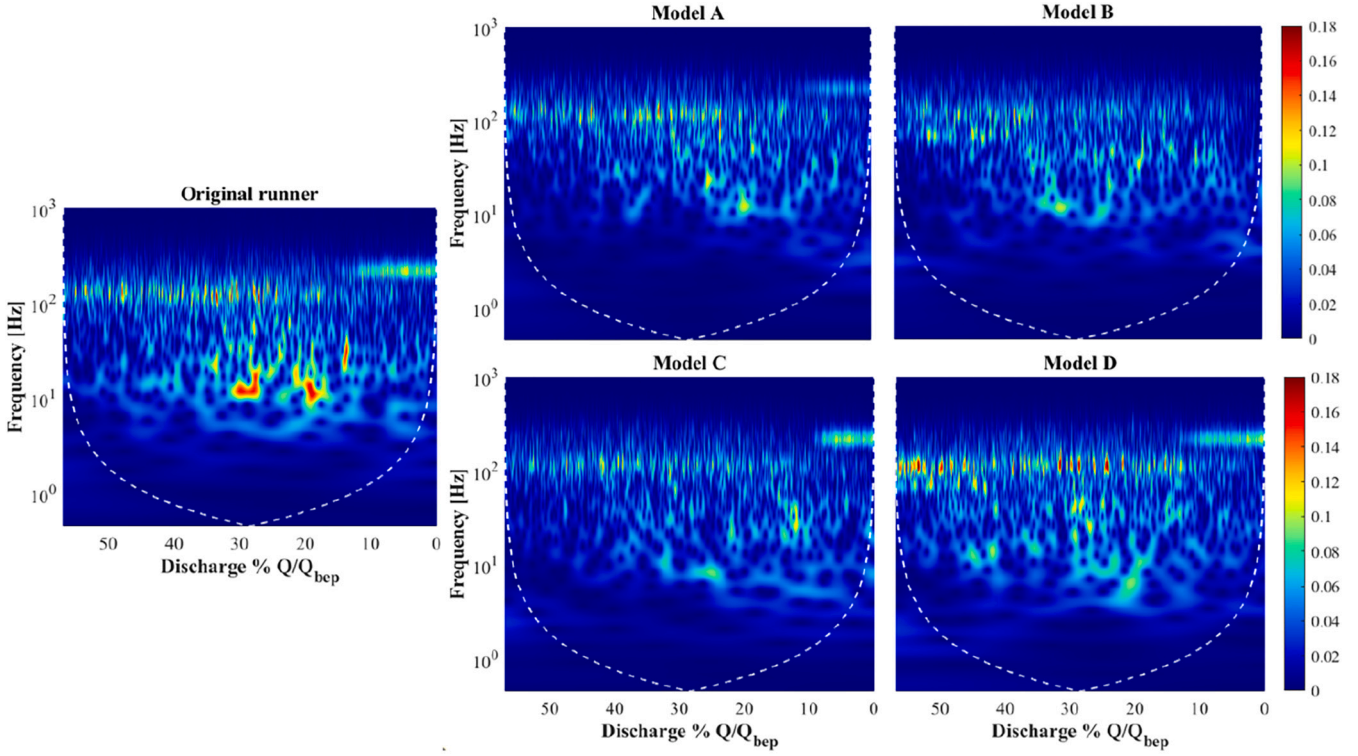

Fig. 14. Continuous wavelet transforms comparison of the water head.

With a similar behaviour, runners model C and D manifests the same perturbation respectively starting from 8%Q_{bep} and 11%Q_{bep}. At the same time, runner model A manifests a reduced amplitude perturbation, within the same frequency band, approximately starting from 10%Q_{bep}. Moreover, original runner and model D shows the greater sensitivity to the stay vanes BP frequency (110 Hz) manifesting, at the same time, the presence of significant low frequency perturbations, associated with the runner rotational speed (10 Hz) in a discharge range between 30 and 20%Q_{bep}.

On the contrary, the wavelet spectrum of rummer model B do not shows signifying disturbances above the stay vanes rotor stator BP frequency (110 Hz).

However, it is important to observe that the complete evolution of structured flow instability occurs predominantly in the latter part of the numerical signals, specifically between 12%Q_{bep} and 8%Q_{bep}. This range is considerably far from the slope variation points of the characteristic curves.

Fig. 15 reports the correlation between the machine hydrodynamics and flow unsteadiness, marking the slope variation and inception of instability in the dimensionless speed and discharge factor plane. The water head signals, filtered by the adoption of a moving mean filter to indicate the overall trend, reveal that slope variation occurs at 21%Q_{bep}, 22.5 %Qbep, 24.3%Q_{bep}, 21%Q_{bep}, for the original runner, models A, B, C, respectively.

Analysis of Fig. 15 clarifies how the beginning of rotating instability (red line) corresponds with an increase in characteristic slope variation. This peculiar pattern is distinctly observable in the original runner and models A, C, and D. In contrast, runner model B characteristic appears to be more homogeneous with an almost constant slope before and after the curve knee-point (blue line).

Nevertheless, it should come as no surprise that rotating instability occurs only in the latter portion of the signals. Indeed, rotating stall often happens when a hydraulic machine operates at flow rates significantly lower or higher than its design point. Under these conditions, the flow angles at the rotor inlet can deviate substantially from optimal values, leading to disturbed flow patterns. Flow separation at the runner inlet section, combined with the reduced flow inertia associated with low discharge values, causes the onset of severe flow detachment and backflows.

The blocking effects associated with the onset of flow recirculation in a runner channel cause the flow to deflect, increasing the incidence angle at the subsequent runner blade. Simultaneously, the discharge increases in the previous runner channel, thereby decreasing the flow detachment. As a result, the stall cell tends to move in a direction away from the oncoming flow.

According to the machine water head spectral content (Fig. 10) and wavelet analysis (Fig. 14), it is possible to assert how the rotor-stator interaction between the guide vanes and the structured rotating instability represents the main source of hydraulic excitation during the turbine brake operating condition.

The correlation between the high frequency perturbation occurring in the last portion of the signals and the onset of a structured rotating instability is also confirmed by the wavelet analysis of the torque acting on a single runner blade (Fig. 16). Here, the torque perturbation associated with the onset and development of the rotating instability in the runner appears in the original geometry with a characteristic frequency of 3.3 Hz starting from 16%Q_{bep}. The BPF frequency (220 Hz in the rotating frame), with more or less constant amplitude in the entire simulation, is also captured in the wavelet analysis of the runner blade signal, but its intensity in the time-frequency domain is much less significant compared to the rotating instability one. Hence, the rotating stall presents the dominant frequency perturbation, even if limited in time due to its development in the last part of the signals.

Likewise, runner model A and D presents a high amplitude signal perturbation starting respectively at 18%Q_{bep} and 15%Q_{bep} at a frequency of 3.3 Hz and 3.5 Hz. Runner model C appears to be less susceptible toward the development of the flow instability with the onset of the low frequency perturbation starting from 10%Qbep with, at the same time, lower amplitude compared to the original, model A and D runners. Finally model B shows only a disturbance around 3hz in the last portion of the signal with a significantly smaller intensity, testifying the lower sensitivity of the geometry on the full development of the rotating stall phenomenon.

In order to highlight the different sensitivity of the various runner geometries to rotating instability, Fig. 17 shows the variation of the torque acting on the runner blades with respect to the average blade torque value according to the following equation:

$$T_{F\_bi}(t) = T_{bi}(t) - \frac{\sum_{i=1:7} T_{bi}(t)}{N_b} \tag{7}$$

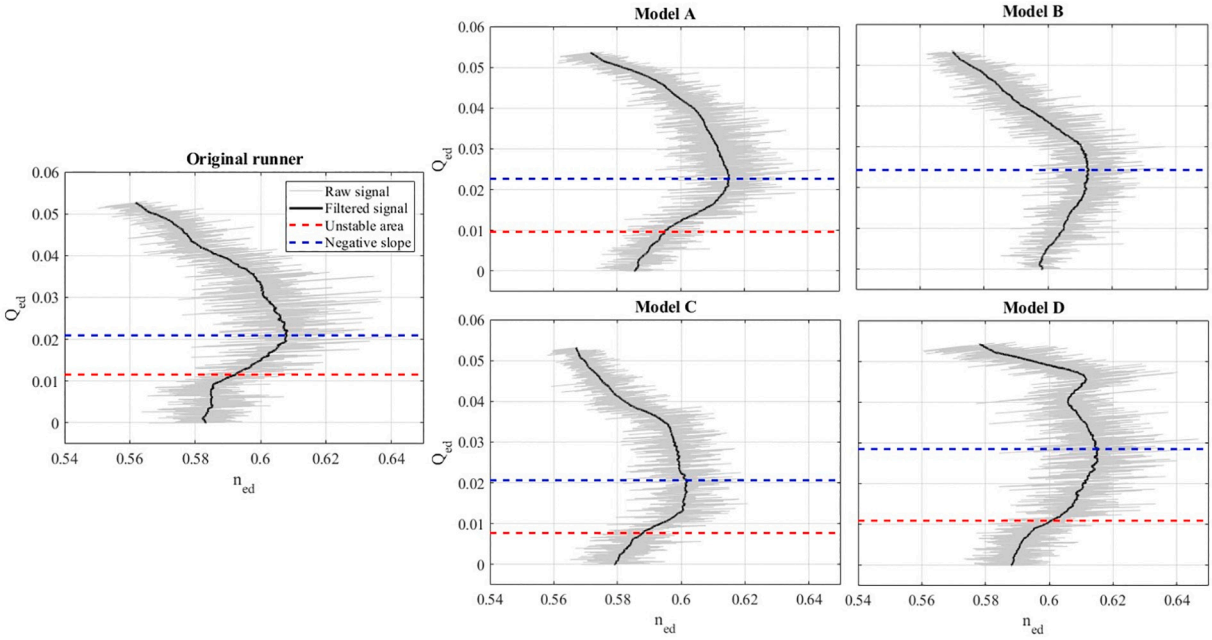

Fig. 15. Filtered non-dimensional machine characteristic curves comparison for different runner lean-angle configurations: slope variation point and unstable area.

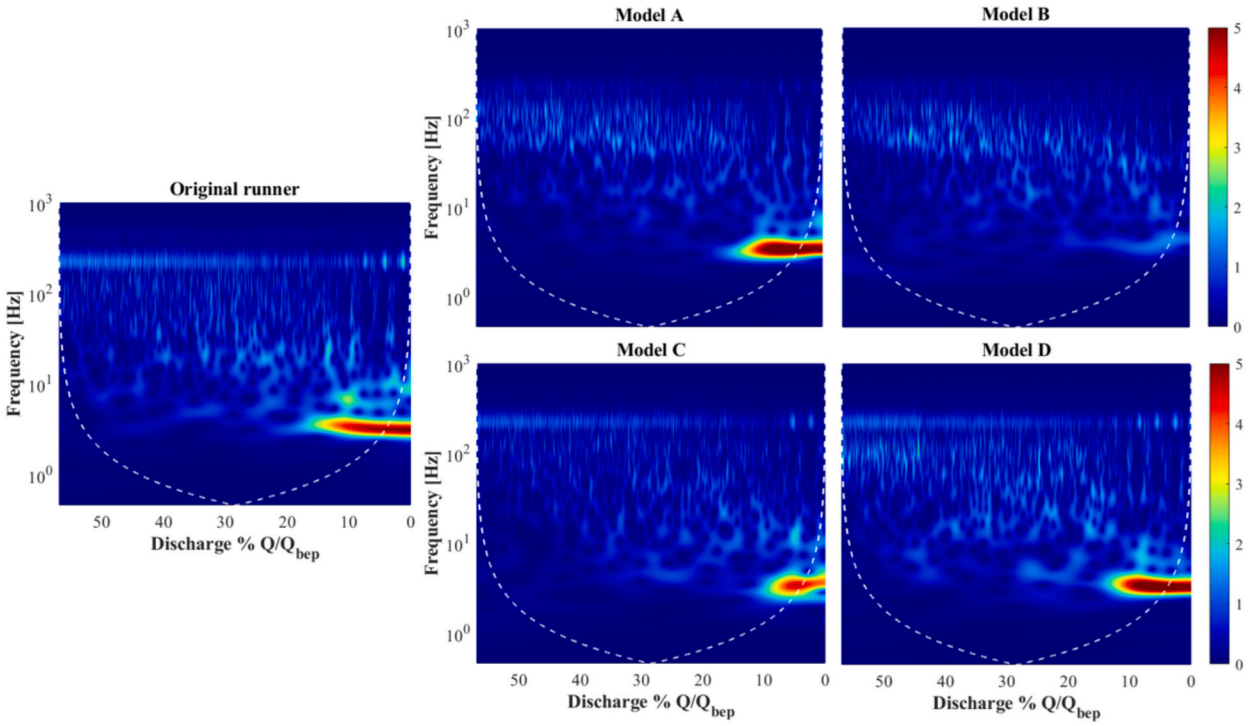

Fig. 16. Continuous wavelet transforms comparison of the torque acting on a runner blade (RB1).

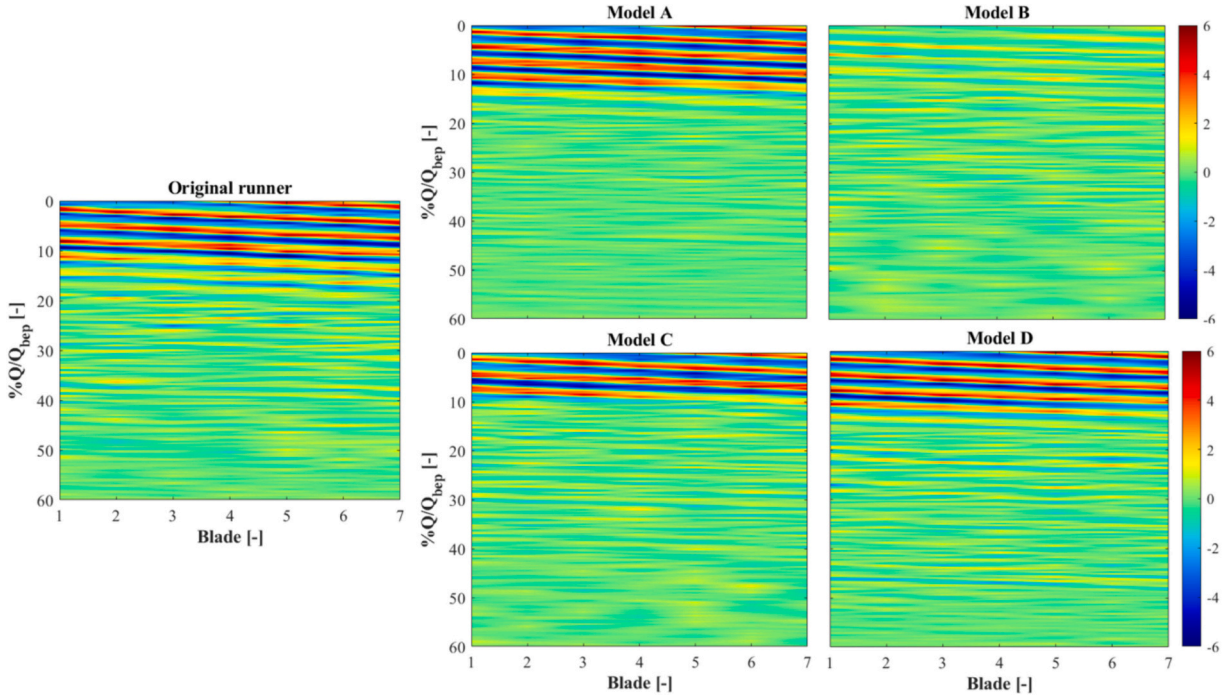

Fig. 17. Evolution of the instantaneous z-torque acting on the runner blades.

where $T_{F\_bi}(t)$ represents the instant filtered torque acting on the i-th runner blade. Thanks to this approach it has been possible to compensate the time-progressive decline of the blade torque thus returning a value fluctuating around a zero mean.

As it can be seen in Fig. 17, the rotating instability affecting the original runner geometry moves from one channel to the subsequent against the runner rotation direction with almost constant amplitude starting around from 18%Qbep. Within this contest, each runner blade torque alternates between positive and negative values according to the rotation frequency of the instability.

Only runner model B appears to be free of periodic unstable phenomena with only an almost negligible increase in torque fluctuation in the last portion of the signal.

5. Fluid flows comparison

The previous analysis allowed to identify the influence of the runner blade lean angle on the evolution of the stress acting on the machine in the unstable operating area. While the spectral and time-frequency characterization of the numerical results showed a strong relationship between the runner blade lean configuration and the machine hydrodynamic instability in the turbine brake area, it is still unclear how the runner geometrical configuration affects the fluid flow, especially during the onset and development of the rotating stall phenomenon.

Because of this, a comparative analysis was performed between the original and model B runners, which exhibit notably different behaviors, particularly in the turbine brake area. Fluid trajectories, pressure contours, and instantaneous velocity fields inside the runner and guide vanes were compared at two different flow rates: 55%Q_{bep} (OP1 - partial load safe operating condition) and 8%Q_{bep} (OP2 – turbine brake area), which were considered most representative. On one side, the comparison of the behaviour under stable conditions can allow to identify the existence (or not) of potential precursors related to the development of instability (Fig. 18a). On the other side, an operating point in the turbine brake area can allow to highlight the different behaviour, testified by the more intense amplitude of the forces acting on the runner (Fig. 18b).

Looking at the flow fields, in OP1, the flow is sufficiently stable and guided both for the original runner (Fig. 19a) and model B geometry (Fig. 19b). Small detachment areas are visible near the blade pressure sides for both configurations, probably caused by the high relative flow incidence angle due to the partial load operating condition. It is interesting to notice that the fluid field in the runner model B is still almost axial-symmetrical whereas the one in the original runner has already lost this symmetry, with some runner channels affected by large detachment areas and other by the onset of secondary flows.

In OP2, while the fluid and pressure fields in the model B geometry are perturbed by small recirculating areas partially altering the axial symmetry without clear signs of the onset of an organized structure (Fig. 19d), the original runner clearly shows the presence of the rotating instability (Fig. 19c). Large recirculating area affect some runner and guide vane channels, causing a clear increase in pressure on the pressure side of the guide vanes located in correspondence of the choked runner channels.

Another difference between the geometries is highlighted in Fig. 20 reporting the velocity streamlines and the pressure distribution at 20 % span (blade-to-blade view) in OP2. An intense backflow, flowing back from the draft tube into the runner, affects the original geometry at the outlet section.

The original runner exhibits intense backflow in three consecutive impeller channels, namely channels 3, 4, and 5, during the full development of the rotating stall phenomenon.

In the guide vanes, the blocking effect associated with the runner backflows simultaneously affects more than one channel. The rotating instability moves, in accordance with the runner rotation direction, from one channel to the next, displaying the typical characteristics of the rotating stall phenomenon (RS).

It is also interesting to notice that, in the guide vanes chocked channels, the static pressure between the inlet and the outlet increases, contributing to the increase in the RPT head and hence to the change in slope of the characteristic curve. The correlation between the development of the rotating stall and the water head it is further demonstrated in Fig. 10 where the interaction between the guide vanes is related to the presence of the perturbations occurring in the frequency band within 216.5 Hz and 216.6 Hz.

This backflow, which is strongly correlated with the instability development [17], is not present in the runner model B, confirming the positive influence of the lean distribution on the fluid-dynamic stability inside the runner. Only minor backflows occur at the outlet section and no related sensitive pressure perturbations occur in the guide vanes.

Finally, to better appreciate the differences in hydrodynamic behaviour between the original and the runner model B, the pressure distributions at three different spanwise locations (15 %, 50 % and 85 %) were evaluated at the runner inlet and outlet sections for operating points OP1 and OP2 along circular lines disposed in the stationary frame as showed in Fig. 21. The pressure distributions are reported in Fig. 22 in polar coordinates: the θ-coordinate represents the angular position of the pressure probe along the circular line at the different spanwise locations (15 %, 50 % and 85 %) while the radial-coordinate defines the static pressure value expressed in kPa.

At partial load (OP1), the runner blade passage pressure pulsation is clearly visible at the inlet section in both geometries, although the peaks are less pronounced in the runner model B (Fig. 22a, c). In particular, the blade passage pressure perturbation is more intense at 15 % span in the original runner, whereas for the runner model B it is more pronounced at the 85 % span section in the runner model B and less at 15 % span.

At the outlet, the blade trailing edge proximity is more evident in the original geometry with a concentrated pressure increase/decrease due to the passage from the pressure to the suction side (PS, SS) (Fig. 22b). Even in this case, an intense variation in the pressure field occurs at the 85 % span section for the runner model B.

At partial load (OP1), the runner blade passage pressure pulsation is clearly visible at the inlet section in both geometries, although the peaks are less pronounced in the runner model B (Fig. 22a, c). In particular, the blade passage pressure perturbation is more intense at 15 % span in the

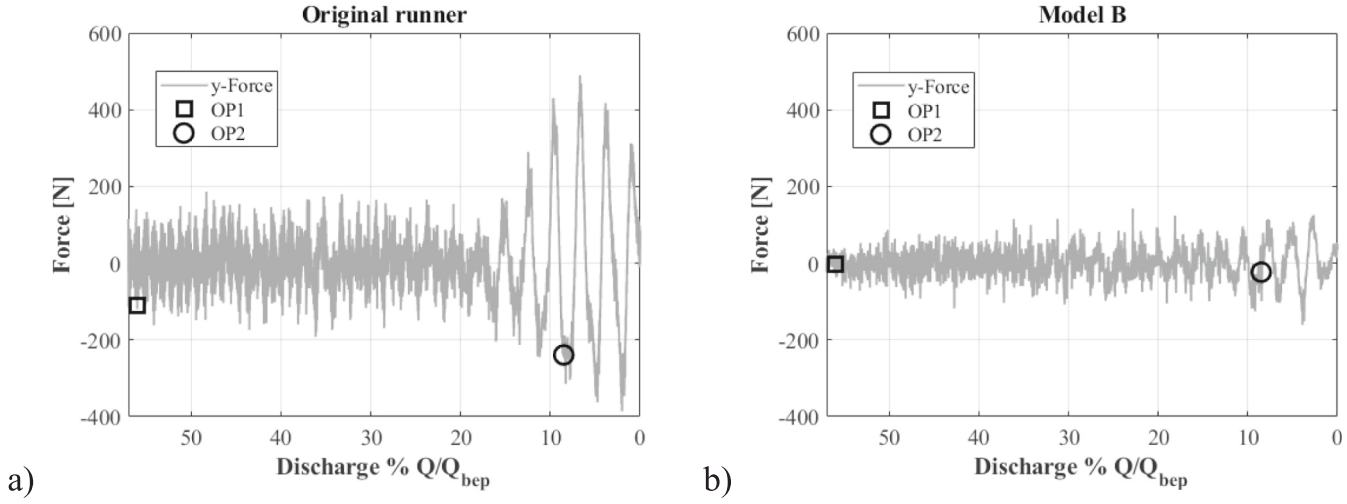

Fig. 18. Evolution of the y-direction radial forces acting on the runner toward the zero-discharge condition: a) Original runner; b) runner model B.

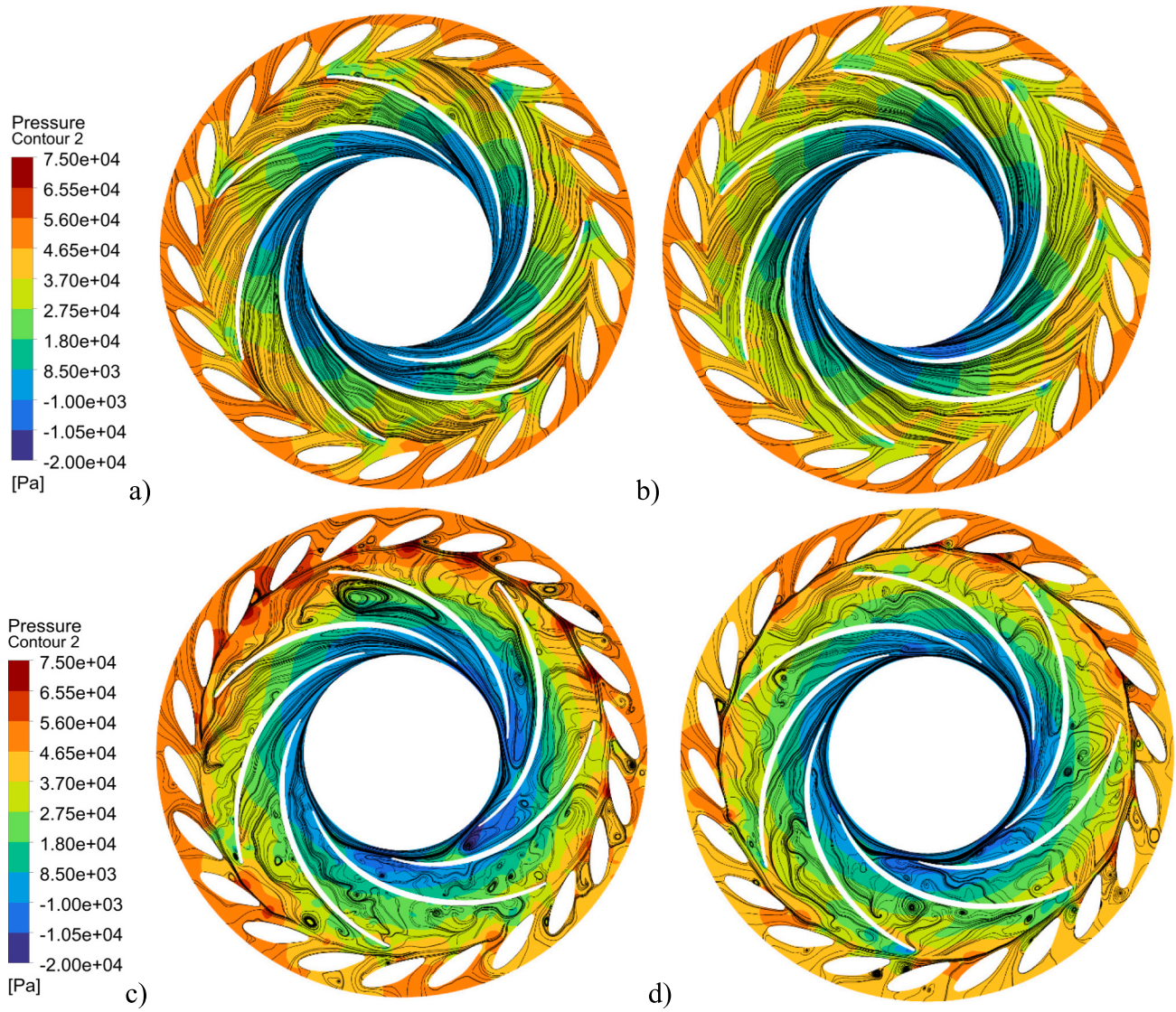

Fig. 19. Instantaneous pressure filed and velocity streamline comparison at the runner (relative streamline) and guide vanes (absolute streamline) midspan section at two different instants: a) original runner OP1; b) runner model B OP1; c) original runner OP2; d) runner model B OP2.

original runner, whereas for the runner model B it is more pronounced at the 85 % span section in the runner model B and less at 15 % span.

At the outlet, the blade trailing edge proximity is more evident in the original geometry with a concentrated pressure increase/decrease due to the passage from the pressure to the suction side (PS, SS) (Fig. 22b). Even in this case, an intense variation in the pressure field occurs at the 85 % span section for the runner model B.

Passing to OP2, in the inlet section of the original geometry the strong rotor-stator interaction generates several pressure peaks located in correspondence of the guide vane (Fig. 22e). Moreover, at the outlet, due to the discharge unbalance introduced by the rotating stall in the blade channels, the pressure distribution appears to be severely perturbated in the angular region between 15° and 210°. It is clear in this case that the influence also of the backflow, developing in the entire spanwise direction with however an intensity decrease toward the shroud surface. As result, the strong unbalance of the radial force in the y-direction that occurs in OP2 (Fig. 20a) can be attributable to this specific pressure distribution unbalance.

On the contrary, for the runner model B, the pressure distribution at the runner outlet is slightly unbalanced at 15 % and 50 % where a less intense backflow is developing. This behaviour is in agreement with the radial force spectral and time-frequency results where only minor low frequency perturbations were detected.

As a result, this study demonstrates how adopting a positive lean angle can significantly improve the hydrodynamic behaviour of a reversible pimp-turbine operating at partial loads. Although this result is in accordance with what has been reported in the literature, this study for the first time demonstrates the close correlation between the lean angle of the impeller blades and the onset of reverse flows during operation in the turbine brake area. Indeed, the suppression of the runner black flow is associated with a sensible reduction of the runner torque and radial forces perturbations allowing for a more stable operation within the unstable branch of the characteristic curve. This behaviour represents a key feature essential for rapid machine grid synchronization during the startup procedure.

6. Conclusions

This study rigorously examines the impact of blade lean configurations on the hydrodynamic instability of a reversible pump-turbine operating in turbine mode through the analysis of five distinct runner geometries. Through comprehensive transient simulation, encompassing 60 impeller revolutions with time-variant boundary conditions (variable discharge and fixed rotational speed), the research covers a

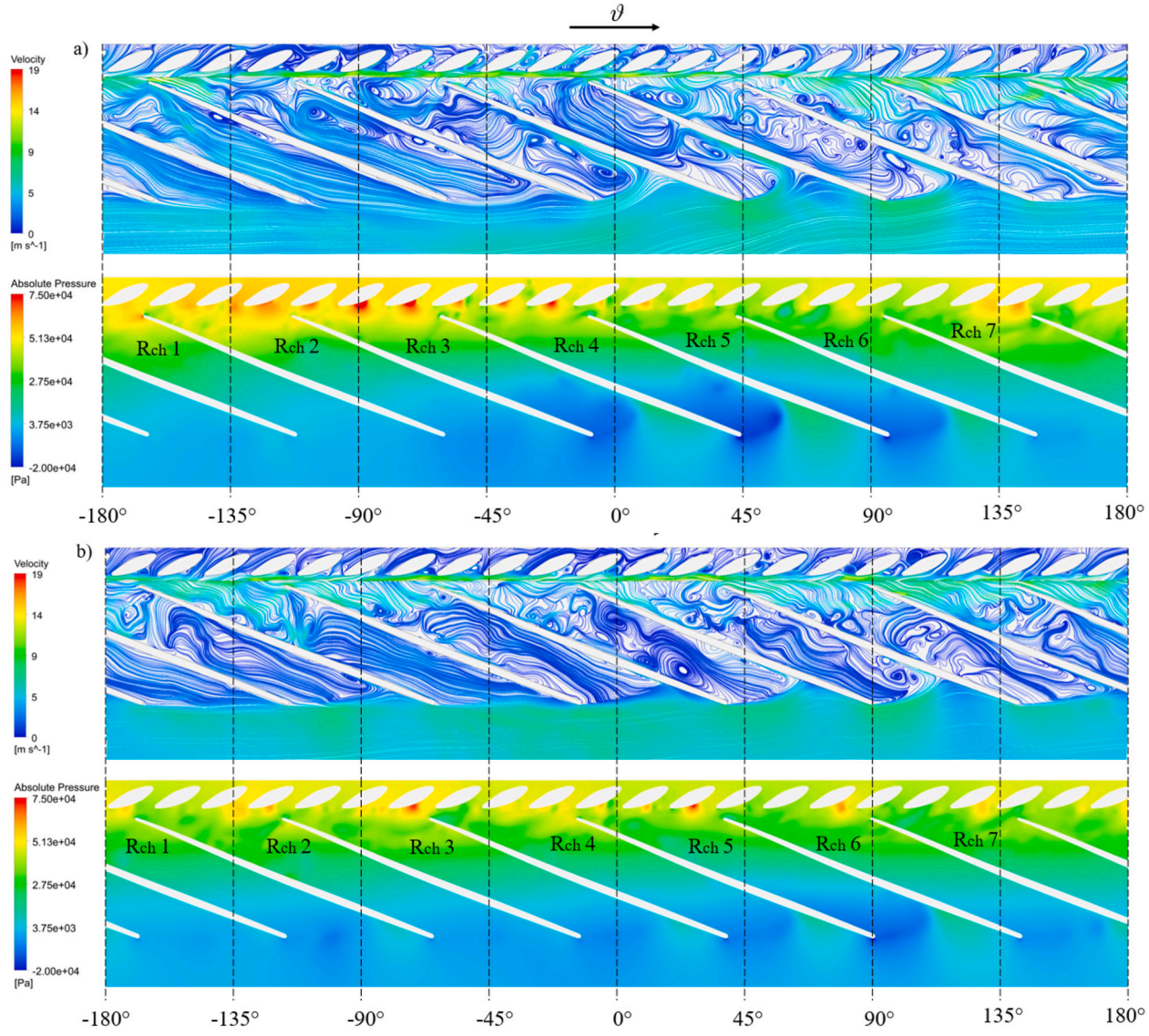

Fig. 20. Instantaneous pressure fields and velocity streamlines in the guide vanes and runner at 20 % span section in the turbine brake operating condition OP2: a) original runner; b) runner model B.

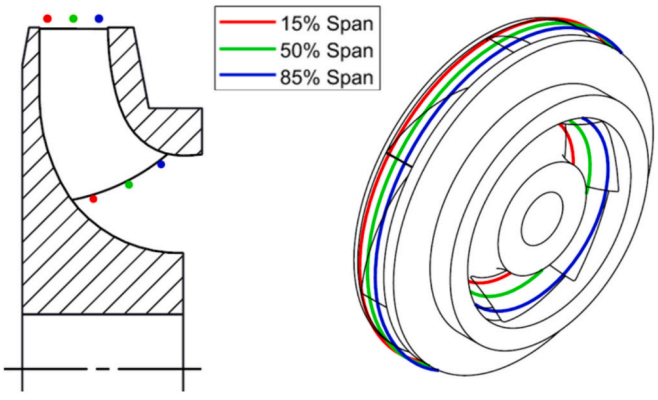

Fig. 21. Inflow and outflow static pressure probe lines location.

broad operational spectrum from stable partial loads to the zero-discharge condition.

Employing a combined spectral, time-frequency, and fluid flow analysis, the hydrodynamic evolution of the turbine toward instability across varying geometries is delineated. This enables a detailed assessment of turbulent structure development and its correlation with characteristic curve slope alterations.

Key insights from the investigation include:

- The rotating stall phenomena were universally observed across all configurations, though their intensity varied. However, the lean angle exhibited minimal effect on the stall's rotational frequency, maintaining between 64 % to 67 % of the impeller rotational speed across configurations;
- The blades lean angle significantly influenced the rotor-stator interactions, with varying intensities of pressure pulsations impacting the machine's water head. Notably, the 0° lean configuration experienced the most pronounced pressure pulsations;
- Severe radial force pulsations, linked to the onset of large recirculation areas during turbine brake operation and runner discharge imbalance, were detected in four of the five configurations;
- A 15° positive linear lean angle on runner blades was found to markedly enhance stability in turbine brake conditions, noticeably mitigating pressure and radial force perturbations. In detail, the runner back-flow suppression occurring in the turbine brake area has

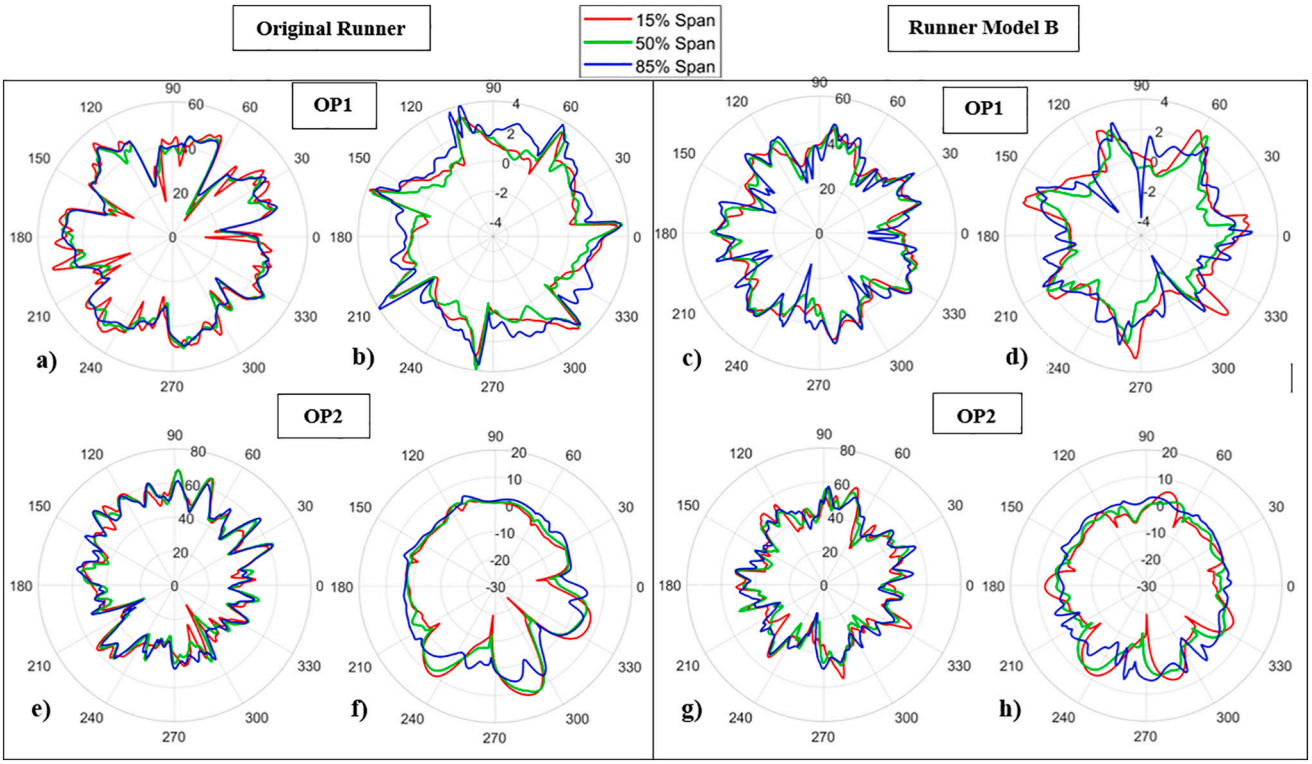

Fig. 22. Pressure distributions at the runner inlet and outlet section: a,e) original runner inlet section; b,f) original runner outlet section; c,g) runner model B inlet section; d,h) runner model B outlet section.

been found to play a key role guaranteeing a more uniform pressure and fluid field.

In conclusion, while a negative curved lean provides marginal improvements in radial forces and pressure pulsations, a pronounced positive runner blade lean angle significantly enhances stability, mitigating the adverse effects associated with the full development of rotating stall phenomena. Despite this, variations in the slope of the characteristic curve persisted across all configurations. Nonetheless, a significant positive lean angle was effective in reducing pressure and force perturbations, with the presence of rotating stall still detectable.

Despite the adoption of large positive runner blade angle is not able to fully suppress the s-shaped characteristic, the drastic reduction of the runner torque and radial forces perturbations in the turbine brake area could lead to a faster machine grid synchronization during the startup procedure.

This characterization, if extended to other main geometrical parameters of the runner, represents a crucial starting point for the development of new design strategies aimed at providing maximum flexibility for units and plants.

Nomenclature

b	Impeller or guide vanes width	mm
$BPF = \frac{n_r n}{60}$	Blade passage frequency	Hz
BP	Blade pass	–
Cb	Cosine bell windowing function	–
D	Diameter	mm
$F_{x,y}$	x, y direction radial forces	N
Fr	Modulus of the radial force	N
F_z	axial force	Axial forcw
g	Gravitational acceleration	m/s^2
H	Water head	m
n	rotational speed	rpm
N	Blades number	–

(*continued on next column*)

(*continued*)

$n_{ED} = \frac{nD_2}{\sqrt{E}}$	speed factor	–
$n_s = \frac{nQ^{0.5}}{h^{0.75}}$	Specific speed	–
p	Pressure	Pa
Q	Discharge	m3/s
$Q_{ED} = \frac{Q}{2D_2^2\sqrt{E}}$	Discharge factor	–
r	Cosine factor	–
t	Time	s
T	Torque	Nm
u,v,w	Absolute velocity components	m/s
W(f(t),Ψ(t))	continuous wavelet function	–
Zr	Number of impeller blades	–
Zrc	Number of return channel blades	
Zg	Number of guide vanes	–

Greek symbols

α	guide vanes angle	deg
β	Runner blade angle	deg
ϵ_r	Degree of reaction	–
θ	angular-coordinate	deg
Ψ(t)	Wavelet function	–

Abbreviations

BEP	Best efficiency point
BPF	Blade passage frequency
FFT	Fast Fourier transform
GV	Guide vanes
LES	Large eddy simulation
MGV	Misaligned guide vanes
OP1,2	Partial load, turbine brake operative points
PHES	Pumped hydro energy storage
RMS	Root mean square
RPT	Reversible pump turbine

(*continued on next page*)

(*continued*)

RS	Rotating stall
RANS	Reynolds average Navier Stoke
SAS	Scale adaptive simulation
SST	Shear stress transport
URANS	Unsteady Reynolds average Navier Stokes

Subscripts

b	Blade
bep	Best efficiency point
F	Filtered
GV	Guide vanes
H	Water head
h	Hydraulic
RC	Return channel
RI	Rotating instability
RF	Rotating frame
RR	Runner Rotation
SF	Stationary frame
1	Runner outlet section
2	Runner inlet section
3	Guide vanes inlet section
4	Return channel outlet section

CRediT authorship contribution statement

Giacomo Zanetti: Writing – review & editing, Writing – original draft, Visualization, Validation, Methodology, Investigation, Formal analysis, Data curation, Conceptualization. **Giovanna Cavazzini:** Writing – review & editing, Writing – original draft, Visualization, Validation, Supervision, Resources, Project administration, Methodology, Conceptualization. **Alberto Santolin:** Writing – review & editing, Resources, Methodology, Funding acquisition. **Francesco Nascimben:** Writing – review & editing, Investigation.

Declaration of generative AI and AI-assisted technologies in the writing process

During the preparation of this work, the authors used Chat GTP 3.5 to improve in clarity and readability of the material. After using this tool, the authors reviewed and edited the content as needed and take full responsibility for the content of the publication.

Declaration of competing interest

The authors declare that they have no known competing financial interests or personal relationships that could have appeared to influence the work reported in this paper.

Data availability

Data will be made available on request.

References

[1] EU Commission. Report on a Comprehensive European Approach to Energy Storage 2019/2189(INI).

[2] R. Fisher, J. Koutnik, L. Meier, V. Loose, K. Engels, T. Beyer, A comparison of advanced pumped storage equipment drivers in the U.S. and Europe, in: Hydro Vision 2012, Louisville, KY, 2012.

[3] G. Ardizzon, G. Cavazzini, G. Pavesi, A new generation of small hydro and pumped-hydro power plants: advances and future challenges, Renew. Sust. Energ. Rev. 31 (2014) 746–776.

[4] R. Baxter, Energy Storage: A Nontechnical Guide, PennWell, Tulsa, OK, 2006.

[5] L. Soder, H. Abildgaard, A. Estanqueiro, et al., Experience and challenges with short-term balancing in european systems with large share of wind power, IEEE Trans. Sustain. Energy 3 (2012) 853–861.

[6] G. Cavazzini, J.B. Houdeline, G. Pavesi, O. Teller, G. Ardizzon, Unstable behavior of pump-turbines and its effects on power regulation capacity of pumped-hydro energy storage plants, Renew. Sust. Energ. Rev. 94 (2018) 399–409.

[7] A. Rezghi, A. Riasi, The interaction effect of hydraulic transient conditions of two parallel pump-turbine units in a pumped-storage power plant with considering "S-shaped" instability region: numerical simulation, Renew. Energy 118 (2018) 896–908.

[8] E. Egusquiza, C. Valero, D. Valentin, et al., Condition monitoring of pump-turbines. New challenges, Measurement 67 (2015) 151–163.

[9] J.X. Zhou, B.W. Karney, J.C. Xu, Analytical study on possible self-excited oscillation in S-shaped regions of pump turbines, Proc. Inst. Mech. Eng., Part A: J. Power Energy 225 (8) (2011) 1132–1142.

[10] S. Pejovic, Q.F. Zhang, B. Karney, A. Gajic, Analysis of pump turbine S instability and reverse water hammer incidents in hydropower systems, in: 4th Int Meeting on Cavitation and Dynamic Problems in Hydraulic Machinery Systems, Belgrade, Serbia, 2011.

[11] C.E. Brennen, Hydrodynamics of Pumps, Oxford University Press, Oxford, UK, 1994.

[12] F. Botero, V. Hasmatuchi, S. Roth, M. Farhat, Non-intrusive detection of rotating stall in pump-turbines, Mech. Syst. Signal Process. 1-2 (48) (2014) 162–173.

[13] C. Widmer, T. Staubli, N. Ledergerber, Unstable characteristics and rotating stall in turbine brake operation of pump-turbines, ASME. J. Fluids Eng. 133 (4) (May 11, 2011) 041101. April 2011.

[14] V. Hasmatuchi, M. Farhat, S. Roth, F. Botero, F. Avellan, Experimental evidence of rotating stall in a pump-turbine at off-design conditions in generating mode, ASME. *J. Fluids Eng.* 133 (5) (June 7, 2011) 051104. May 2011.

[15] P. Xue, Z. Liu, L. Lu, Z. Gao, X. Meng, Experimental research on the rotating stall of a pump turbine in pump mode, Water 11 (2019) 2426, https://doi.org/10.3390/w11112426.

[16] G. Cavazzini, A. Covi, G. Pavesi, G. Ardizzon, Analysis of the unstable behavior of a pump-turbine in turbine mode: fluid-dynamical and spectral characterization of the s-shape characteristic, ASME. J. Fluids Eng. 138 (2) (2015) 021105. February 2016.

[17] G. Zanetti, G. Cavazzini, A. Santolin, Three-dimensional evolution of the flow unsteadiness in the S-shape of pump-turbines and its correlation with the runner geometry, J. Energy Storage 57 (2023) 106176. ISSN 2352-152X.

[18] P. Xue, Z. Liu, L. Lu, Z. Gao, X. Meng, Experimental research on the rotating stall of a pump turbine in pump mode, Water 11 (11) (2019) 2426.

[19] Y. Zhang, Y. Zhang, Y. Wu, A review of rotating stall in reversible pump turbine, J. Mech. Eng. Sci. 231 (7) (2017) 1181–1204.

[20] Y.X. Xiao, R.F. Xiao, Transient simulation of a pump-turbine with misaligned guide vanes during turbine model start-up, Acta Mech. Sinica 30 (2014) 646–655, https://doi.org/10.1007/s10409-014-0061-6.

[21] G. Zhiwei, W. Chihang, Q. Zhongdong, L. Xianwu, X. Weipeng, Suppression of hump characteristic for a pump-turbine using leading-edge protuberance, Proc. IME J. Power Energy 234 (2) (2020) 187–194.

[22] G. Olimstad, T. Nielsen, B. Børresen, Dependency on runner geometry for reversible pump turbine characteristic in turbine mode of operation, ASME J. Fluids Eng. 134 (12) (2012) 121102.

[23] J. Yin, D. Wang, X. Wei, L. Wang, Hydraulic improvement to eliminate S-shaped curve in pump turbine, ASME J. Fluids Eng. 135 (7) (2013) 0711105.

[24] B. Zhu, L. Tan, X. Wang, Z. Ma, Investigation on flow characteristics of pump-turbine runners with large blade lean, J. Fluid. Eng., Trans. ASME 140 (3) (2018) 031101.

[25] Weixiang Ye, Chen Geng, Xianwu Luo, Unstable flow characteristics in vaneless region with emphasis on the rotor-stator interaction for a pump turbine at pump mode using large runner blade lean, Renew. Energy 185 (2022) 1343–1361. ISSN 0960–1481.

[26] J. Ouyang, Y. Luo, R. Tao, Influence of blade leaning on hydraulic excitation and structural response of a reversible pump turbine, Proc. Inst. Mech. Eng., Part A: J. Power Energy 236 (2) (2022) 241–259, https://doi.org/10.1177/09576509211034964.

[27] J. Yang, G. Pavesi, S. Yuan, G. Cavazzini, G. Ardizzon, Experimental characterization of a pump–turbine in pump mode at hump instability region, ASME. J. Fluids Eng. 137 (5) (May 1, 2015) 051109, https://doi.org/10.1115/1.4029572. May 2015.

[28] Unstable flow characteristics in s-shaped region of pump-turbine runners with large blade lean by Z Ma, B Zhu, C Rao, L Tan, in: Proceedings of the ASME 2017 Fluids Engineering Division Summer Meeting FEDSM2017 July 30–August 3, 2017, Waikoloa, Hawaii, USA, 2017.

[29] Z. Ma, B. Zhu, Pressure fluctuations in vaneless space of pump-turbines with large blade lean runners in the S- shaped region, renew, Energy 153 (2020) 1283e1295.

[30] J. Yang, G. Pavesi, S. Yuan, G. Cavazzini, G. Ardizzon, Experimental characterization of a pump–turbine in pump mode at hump instability region, ASME J. Fluids Eng. 137 (5) (2015) 051109.

[31] T. Krappel, A. Ruprecht, S. Riedelbauch, R. Jester-Zuerker, A. Jung, Investigation of Francis turbine part load instabilities using flow simulations with a hybrid RANS-LES turbulence model, IOP Conf. Ser.: Earth Environ. Sci. 22 (2014) (2014) 032001.

[32] F.R. Menter, Y. Egorov, The scale-adaptive simulation method for unsteady turbulent flow predictions. Part 1: theory and model description, Flow, Turbulence and Combustion 85 (1) (2010) 113–138.

[33] G. Zanetti, G. Cavazzini, A. Santolin, Effect of the von Karman shedding frequency on the hydrodynamics of a Francis turbine operating at nominal load, Int. J. Turbomach. Propuls. Power 8 (2023) 27, https://doi.org/10.3390/ijtpp8030027.

[34] V. Hasmatuchi, S. Roth, F. Botero, M. Farhat, F. Avellan, Hydrodynamics of a pump-turbine at off-design operating conditions: numerical simulation, in: Proceedings of the 7th International Symposium on Pumping Machinery, 2011. Hamamatsu, Japan.
[35] N. Sotoudeh, R. Maddahian, M.J. Cervantes, Investigation of rotating Vortex rope formation during load variation in a Francis turbine draft tube, Renew, Energy 151 (2020) 238–254. ISSN 0960–1481.
[36] G. Cavazzini, G. Pavesi, G. Ardizzon, Pressure instabilities in a vaned centrifugal pump, Proc. IMechE Part A: J. Power Energy 0 (2011) 1–10, https://doi.org/10.1177/0957650911410643.
[37] J. Yang, G. Pavesi, S. Yuan, G. Cavazzini, G. Ardizzon, Experimental characterization of a pump–turbine in pump mode at hump instability region, ASME. J. Fluids Eng. 137 (5) (May 1, 2015) 051109, https://doi.org/10.1115/1.4029572. May 2015.
[38] O. Braun, Part Load Flow in Radial Centrifugal Pumps, EPFL, Lausanne, Switzerland, 2009. PhD Thesis No. 4422.
[39] G. Zanetti, M. Siviero, G. Cavazzini, A. Santolin, Application of the 3D inverse design method in reversible pump turbines and Francis turbines, Water 15 (2023) 2271, https://doi.org/10.3390/w15122271.
[40] G. Pavesi, G. Cavazzini, G. Ardizzon, Time–frequency characterization of the unsteady phenomena in a centrifugal pump, Int. J. Heat Fluid Flow 29 (5) (2008) 1527–1540.
[41] P. Bloomfield, Fourier Analysis of Time Series: An Introduction 2000, WileyInterscience, New York, 2000.
[42] A. Lucius, G. Brennen, Numerical simulation and evaluation of velocity fluctuations during rotating stall of a centrifugal pump, ASME J. Fluids Eng. 133 (8) (2011) 081102.
[43] M. Farge, Wavelet transforms and their application to turbulence, Annu. Rev. Fluid Mech. 24 (1992) 395–457.